transcriptional activation of the *UbC* gene (Fig. 6B). These experiments showed that UCH L1 does not upregulate Ub levels via transcriptional activation.

Second, to address the possibility that a reduction in the release of mono-Ub from poly-Ub or Ub-conjugated proteins affects the level of free mono-Ub in *gad* mice, UCH L1-catalyzed release of mono-Ub from substrates was tested. UCHs can generate mono-Ub from poly-Ub and peptide–ubiquityl amides *in vitro* (12). However, no enhanced intensity corresponding to the release of Ub from poly-Ub (Fig. 3A; compare left and right panels) or mass spectra corresponding to the hydrolysis of peptide–ubiquityl amides (Fig. 1E) was observed in the *gad* mouse immunoprecipitates from brain lysates. Alternatively, an unknown substrate could be upregulated as poly-Ub-conjugated proteins (multi-Ub) in *gad* mice. Therefore, multi-Ub levels were measured in soluble mouse brain lysates by sandwich ELISA using antibody FK2 that is specific for multi-Ub (16–18) (Fig. 6C). No difference in the level of multi-Ub was observed between the wild-type and the *gad* mouse at less than 2 weeks of age. These data argue against the hypothesis that the deficiency in UCH L1-catalyzed release of mono-Ub from multi-Ub is responsible for the decreased level of Ub observed in the *gad* mouse.

Third, the effect of UCH L1 expression on Ub metabolism was examined in MEF cells transfected with either adeno-*Uch l1* or -β-*gal*. Mono-Ub levels were monitored for 30 h after pulse-chase labeling and Ub degradation was compared by autoradiography. Ub half-life was extended in MEF cells transfected with UCH L1 (Fig. 6D). Since lysosomes are implicated as the site of Ub degradation, we examined the effect of the lysosomal inhibitor EST (2,3-*trans*-epoxysuccinyl-L-leucylamide-3-methyl butane ethyl ester) on Ub metabolism (19,20). EST extended Ub half-life in both adeno-*Uch l1*- and adeno-β-*gal*-transfected MEF cells (Fig. 6D) and, under these conditions, mono-Ub degradation was comparable between the adeno-*Uch l1*-transfected cells and the control cells (Fig. 6D).

These data suggest that UCH L1 affects Ub degradation and alters its metabolism, and that Ub degradation occurs in lysosomes.

UCH L1 affinity for Ub appears to be indispensable for the maintenance of Ub levels

To further clarify the effect of UCH L1 on Ub levels, his-tagged *Uch l1* and mutants were transfected into dopamine-producing SH-SY5Y neuronal cells (Fig. 7). UCH L1 and Ub were then visualized using confocal immunofluorescence microscopy. Cells transfected with wild-type *Uch l1* showed a relative increase in Ub immunoreactivity compared with mock-transfected cells (anti-Ub; Sigma, polyclonal; Fig. 7A and E) consistent with Ub upregulation by UCH L1. *Uch l1*^{I93M}, implicated in the pathogenesis of PD, also increased Ub immunoreactivity comparable to wild-type *Uch l1* (Fig. 7B and E). Increased Ub immunoreactivity was also evident in cells transfected with *Uch l1*^{C90S}, which retains Ub binding affinity but lacks C-terminal hydrolase activity (Fig. 7C and E; Table 1) (9). However, significant increase in Ub immunoreactivity was not observed with mutant *Uch l1*^{D30K} (Fig. 7D and E), which carries a charge reversal on the surface of the protein that is presumed to interact with cationic residue of Ub (21). This mutant protein exhibits markedly lower affinity for Ub and has no hydrolase activity (Table 1). These data suggest that UCH L1-mediated increases in Ub levels are a function of UCH L1 affinity for Ub rather than hydrolase activity.

DISCUSSION

In spite of the abundance of UCH L1 in the nervous system and its importance in the neurodegenerative diseases, the *in vivo* functions of UCH L1 have been remained unknown (6–13). The *gad* mouse and the UCH L1 transgenic mouse revealed a novel role for UCH L1 in neurons. Our data indicate that UCH L1 is associated with mono-Ub and elevates the level of mono-Ub in neuron. Previously, Doa4, a deubiquitinating enzyme belonging to UBPs, was reported to elevate the level of Ub in yeast, although the association of Doa4 with Ub was not mentioned (19). From a genetic complementation study, Doa4 was inferred to be involved in endosomal–lysosomal pathway (20). Our pulse-chase labeling using MEF cells suggests that UCH L1 affects Ub metabolism and extends its half-life by inhibiting Ub degradation. As an inhibitor of lysosomal function extended Ub half-life and partially diminished the effect of UCH L1, UCH L1 probably prevents Ub degradation in lysosomes. Thus, our results also suggest the link of DUBs to the endosome–lysomal pathway. Recently, it was demonstrated that Ub itself contains all the necessary signals for both targeting and degradation of monoubiquitylated proteins in the endosomal–lysosomal pathway, with the crucial Ub residues being Gln2, Phe4, Lys6, Leu8, Val26, Leu43, Ile44, Glu64 and Val70 (22,23). Possibly some fraction of free Ub itself is shunted into the endosome–lysosomal pathway and UCH L1 binding to Ub may suppress this route by masking Ub residues that are requisite for targeting. Alternatively, it may be possible that UCH L1 deubiquitylates ubiquitylated proteins before degradation within the endosome–lysosome pathway. However, UCH L1^{C90S}, lacking hydrolase activity, still retains the ability to maintain Ub levels, suggesting that physical association with UCH L1 rather than its deubiquitylating activity promotes Ub stability. Although UCH L1 can very slowly cleave poly-Ub and Ub-small molecule adducts *in vitro* (4), we did not find accumulation of such Ub species in *gad* mice. This finding may reflect functional redundancy between UCHs and UBPs. Alternatively, such Ub species may be detergent insoluble and exist within aggregates of Ub in dot-like structures observed in *gad* mice (10).

It has been long known that Ub-containing protein aggregates as hallmarks of various neurodegenerative conditions (2). Such aggregates are remnants of inadequate proteolysis and suggest either surpluses of aggregation-prone abnormal proteins or insufficiencies in Ub-dependent proteolysis (Fig. 8). PD caused by A53T and A30P mutations of α-synuclein appear to be the examples for the former case. These mutant proteins are more stable than wild-type and presumed to surpass the critical concentration of α-synuclein for oligomerization (24,25). The latter case appears to account for both a *Uch l1* gene deletion in the *gad* mouse and the parkin gene mutations in the patients with PD. Loss of function mutations in Parkin E3 ligase may prevent this enzyme from properly ubiquitylating putative

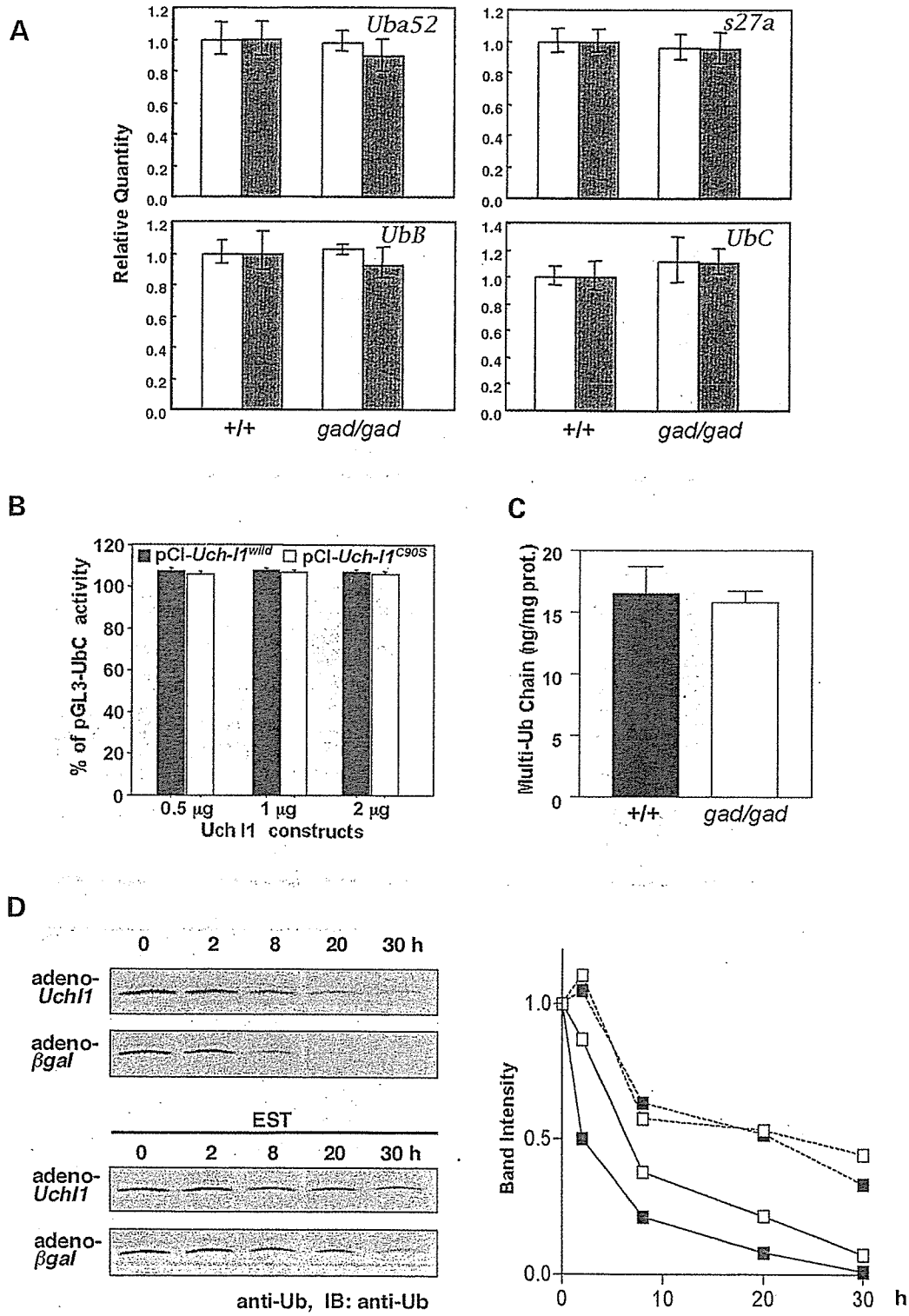

Figure 6. Effects of UCH L1 on transcription, processing and post-translational state of ubiquitin. (**A**) Quantitative RT–PCR for *Uba52*, *s27a*, *UbB* and *UbC* was performed using total RNA from wild-type and *gad* (*gad/gad*) cerebrum ($n = 3$). Mean values are shown with SEM. β-Actin (open bar) or GAPDH (solid bar) were used as internal controls. (**B**) Dual luciferase assay of a vector containing the +18 to +1227 bp region of the human Ub C promoter (pGL3-*UbC*) co-transfected with either UCH L1 (pCI-neo-*Uchl1*^{WT}; solid bar) or an active site mutant of UCH L1 (pCI-neo-*Uchl1*^{C90S}; open bar). Mean values from eight independent experiments are shown with SEM. (**C**) Levels of multi-Ub chain (conjugated poly-Ub) in cerebellum cytosolic fractions were measured by ELISA from 2-week-old mice ($n = 6$) (16–18). Mean values with SEM are shown as filled (+/+) or open (*gad/gad*) bars. (**D**) Adeno-*Uchl1*-transfected or adeno-β-*gal*-transfected MEF cells were labeled with [^{35}S]-Met. Autoradiograms of anti-Ub immunoprecipitates pulse-chased at the indicated times in the absence (left upper panels) or presence of EST (2,3-*trans*-epoxysuccinyl-L-leucylamide-3-methyl butane ethyl ester; left lower panels) are shown. Relative band intensities are quantified and mean values of two independent experiments are shown (right).

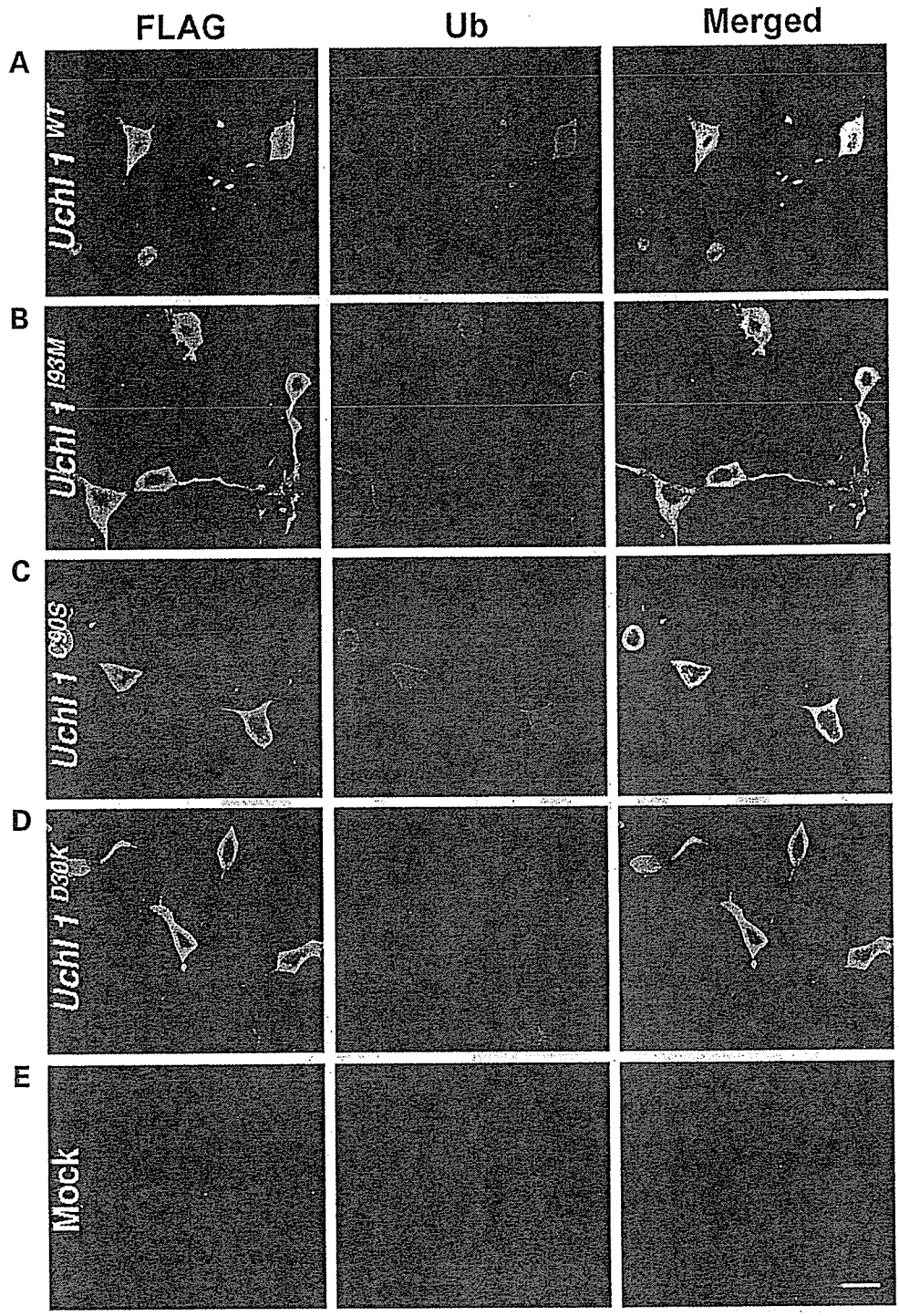

Figure 7. Effect of UCH L1 mutants on ubiquitin expression. Plasmids pcDNA3-*Uchl1*^{WT} (**A**), -*Uchl1*^{I93M} (**B**), -*Uchl1*^{C90S} (**C**), -*Uchl1*^{D30K} (**D**) and vector alone (**E**) were transfected into SH-SY5Y cells and expressed. Antibodies against flag-tag and Ub (Sigma, polyclonal) were used to detect transfected UCH and endogenous Ub, respectively. The faint green staining (left panels) reflects non-specific staining of cells that escaped transfection. Scale bars, 20 μm.

substrates (26,27), causing substrate accumulation and toxicity to neurons at the substantia nigra. Loss of functional UCH L1 could also lead to inadequate ubiquitylation via decrease of free Ub. An initial pathological lesion begins at the synapse of the sciatic nerve in the *gad* mouse. Ub is known to be transported over long distances via slow axonal transport to synapse (28). Ub decrease and the consequent inadequate ubiquitylation of proteins may trigger increased levels of proteins that should undergo Ub-dependent degradation, resulting in the accumulation of such proteins within spheroids observed in *gad* mice (11). The *gad* mouse phenotypes resemble those of Charcot–Marie–Tooth diseases (CMT) in humans. Although there are no

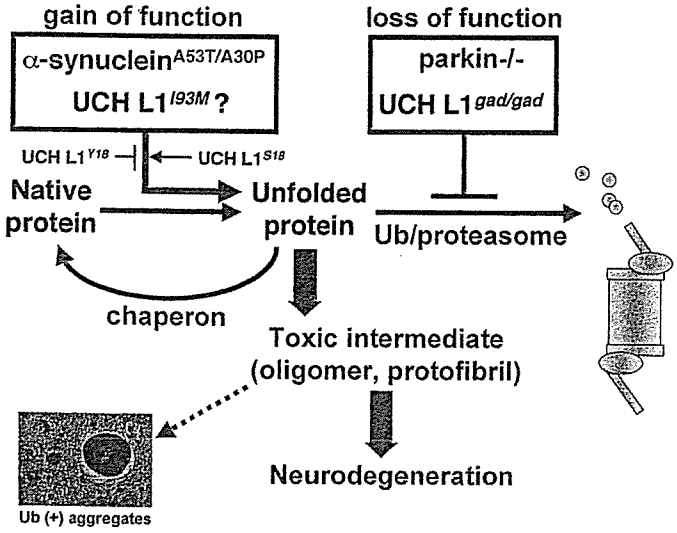

Figure 8. Common pathway of neurodegeneration. Unfolded proteins are refolded by molecular chaperons or degraded by the ubiquitin/proteasome pathway. The red boxes illustrate that excessive production of insoluble proteins by genetic defect (such as A53T/A30P mutations of α-synuclein in Parkinson's disease) or insufficiencies in the ubiquitin/proteasome pathway (such as *Uch l1* gene deletion in the *gad* mouse and the parkin gene mutations in the patients with PD) alter the proportion of denatured proteins within the cell. The accumulation of a toxic intermediate (oligomer or protofibril) is proposed to precede and promote neurodegeneration.

CMT or peripheral neuropathies that map to the proximity of the human *UCH L1* locus so far, immunohistological profiling of UCH L1 and Ub in peripheral nerves would be helpful in delineating a human *gad* analog.

Human *UCH L1* deletion mutants have not been reported although polymorphism and missense mutations of UCH genes are linked to PD (29–32). In idiopathic PD, particularly of Japanese or Chinese origin, UCH L1 gene polymorphism at position 18 is linked to a disease susceptibility (29–32). The S18Y mutation is common in Japanese and Chinese compared with Europeans and is reportedly protective for PD (19–32). Recently, UCH L1 was found to exhibit dimerization-dependent ubiquityl ligase activity at Lys63 of acceptor Ub molecules *in vitro* (13). Polyubiquitylated proteins linked to Lys48 of Ub are destined for proteasomal degradation, while those linked to Lys63 of Ub are stable. The protective variant Y18-UCH L1 exhibits diminished dimerization and ligase activities relative to S18-UCH L1, and therefore Y18-UCH L1 is predicted to accelerate degradation of proteins such as α-synuclein by making less stable species conjugated to Lys 63 of Ub. Thus, the decreased susceptibility to PD in individuals carrying the S18Y mutation could be explained by the low concentration of α-synuclein, which is yet confirmed *in vivo* (13) (Fig. 8). The I93M mutation in UCH L1 is reported in familial PD with dominant inheritance (9). α-Synuclein (dominant form) or the of parkin or DJ-1 (recessive forms) may also cause familial PD (33–35). The glycosylated form of α-synuclein is a substrate for parkin (36). Our present data indicate that UCH L1 upregulates Ub levels *in vivo*, and therefore UCH L1, parkin and α-synuclein appear to be interrelated with respect to Ub and ubiquitylation pathways. As with α-synuclein, the loss of UCH L1 function does not appear to cause PD (11,37). In patients carrying the UCH L1 mutation I93M, both ligase and hydrolase activities are presumed to be partially reduced (9,13). Our data show that UCH $L1^{I93M}$ enhances Ub immunoreactivity similar to UCH $L1^{WT}$ in transfected cells. Moreover, we did not find evidence for nigrostriatal dopaminergic pathology in either *gad* mouse heterozygotes or homozygotes. Therefore, an as yet unknown 'gain of toxic function' condition may underlie PD in patients carrying UCH $L1^{I93M}$ (Fig. 8).

Our results reveal that the fundamental defects in the *gad* mouse are due to a lack of UCH L1 and consequent Ub decrease. Ub and Ub-dependent proteolysis are involved in nearly all cellular processes and therefore it is likely that *gad* mice exhibit a wide variety of neuronal malfunctions that are not recognized by routine histology. Thus, in light of our present data we are currently re-evaluating *gad* mouse phenotypes including behavior, neuronal regeneration and apoptosis. These studies will broaden our understanding of the role of Ub pathways in neuronal function and neurodegenerative disorders.

MATERIALS AND METHODS

Plasmid and protein purification

Sequences encoding UCH L1 were amplified from a mouse brain cDNA library by polymerase chain reaction (PCR), and subcloned into either pQE-30 (Qiagen, Valencia, CA, USA) or pcDNA3 (Invitrogen, Groningen, The Netherlands) for expression in *E. coli* (for protein purification) or mammalian cells (for transfection), respectively. cDNA encoding UCH $L1^{gad}$ was obtained from a *gad* mouse brain by PCR. Another UCH L1 mutations were introduced by PCR-based site-directed mutagenesis (QuickChange Site-Directed Mutagenesis Kit, Stratagene, La Jolla, CA, USA) of template plasmids using primers designed to introduce specific mutations (D30K, C90S, I93M). Proteins overexpressed in *E. coli* were purified using Ni-agarose (Qiagen) as per the manufacturer's protocol and purified further by gel filtration using a Hi Load™ 16/60 Superdex 75 column (Amersham Pharmacia, Uppsala, Sweden).

Generation of adeno-vectors, antibodies and Ub level determination

Recombinant plasmids containing adeno-*Uch l1* and -β-*gal* were constructed using the Adenovirus Expression Vector Kit as per the manufacturer's instructions (Takara, Tokushima, Japan). Briefly, *Uch l1-flag* and β-*gal-flag* genes were inserted individually into the cosmid vector pAxCANLw containing the CAG promoter, the stuffer sequence and two loxP sequences. These recombinant cosmids were co-transfected into HEK 293 cells with a restriction enzyme-digested adenovirus DNA-TPC to generate a recombinant adenovirus through homologous recombination. Expression of the *Uch l1*- or β-*gal*-gene is achieved by removal of the stuffer sequence between the loxP sequences by Cre recombinase (expressed by co-transfection with pAx CANCre DNA).

Immunizing with different ubiquitin-carrier conjugates produced five antibodies and, among them, US-1 was found to be specifically reactive to mono-Ub (16). Immune complexes of US-1 and ^{125}I-mono-Ub were obtained by centrifuge and counted in a gamma counter. The inhibition for the tracer bound to the antibody in the presence of lysates was measured and mono-Ub level was determined from the standard curve generated by unlabeled Ub (16). Monoclonal antibody FK2 that recognizes conjugated-multi-ubiquitin chain was used for immunoassay (sandwich ELISA) for multi-ubiquitin chains as described (17,18). This ELISA system shows an only negligible reactivity to free-Ub (17).

Fractionation, immunoaffinity purification and immunoblotting

Mouse brains were homogenized in lysis buffer (50 mM NaH_2PO_4/300 mM NaCl/10 mM imidazole, containing a complete protease inhibitor cocktail, pH 8.0) and centrifuged at 70 000*g* for 1 h to yield a cytosolic fraction. The nuclear fraction was extracted with lysis buffer containing 10% NP-40 and 400 mM NaCl. Insoluble materials were dissolved with 8 M urea. For pull-down assays, 200 µg of His_6-tagged UCH $L1^{WT, C90S, D30K}$ and 40 µl of Ni-NTA Agarose (Qiagen) were added to 750 µl mouse brain lysate containing 6 mg total protein. After gentle rotation overnight at 4°C, the Ni-NTA beads were washed three times with 200 µl of wash buffer (50 mM NaH_2PO_4/300 mM NaCl/20 mM imidazole, pH 8.0). The beads were eluted with 3 × 40 µl elution buffer (50 mM NaH_2PO_4/300 mM NaCl/250 mM imidazole, pH 8.0) and subjected to SDS–PAGE, stained with Coomassie brilliant blue (CBB) or immunoblotted. Densitiometric analysises were done using software PD QUEST (BioRad). For TOF analysis, 1 µl samples were spotted onto H4 hydrophobic-coated Protein Chip Array (Ciphergen Biosystems, Palo Alto, CA, USA) after desalting with a C_{18} zip tip column. The ionized proteins were detected and accurate mass was determined based on TOF analysis. TOF mass spectra were collected in the positive ion mode and signal averages of 50 laser shots were used to generate each spectrum. After SDS–PAGE on a 10–20% gradient gel, protein bands migrating at ~8 kDa were excised and digested within the gel with trypsin (Sigma). Digested peptide samples were then introduced via nano-spray into a QSTAR Pulsar LC/MS/MS system (Applied Biosystems, Foster City, CA, USA). Immunoblotting was performed as described (10) using antibodies to Ub (1 : 100, Chemicon, MAB1510) and UCH L1 (1 : 1000, Chemicon, polyclonal). The Ub antibody MAB1510 is reactive to both free and conjugated forms of Ub in immunoblotting (15). The epitopes of UCH L1 antibody were confirmed to recognize the region encoded by other than exons 7 and 8 of *Uch l1* gene, by using UCH $L1^{gad}$ protein produced by *E. coli* expression system. Ub and $(Ub)_n$ were purchased from Boston Biochem, MA, USA.

Immunohistochemistry, immunofluorescence and electron microscopy

Twelve-week-old mouse brain and sciatic nerve sections were analyzed by immunocytochemistry as previously described (10) using antibodies to Ub that is predominantly reactive to free Ub in immuno-histochemistry (1 : 100, Sigma) and UCH-L1 (1 : 40, Medac; monoclonal). Antibodies to neurofilament-M (NF; 1 : 200, Chemicon, monoclonal), glial fibrillary acidic protein (GFAP; 1 : 200, Chemicon, monoclonal), proteolipid protein (PLP; 1 : 200, Chemicon, monoclonal) and myelin basic protein (MBP; 1 : 200, QED bioscience, monoclonal) were used as neuronal, astrocytes, oligodendrocytes, schwann cell markers, individually. For immunofluorescence studies, anti-mouse-Cy3 or -FITC or anti-rabbit-conjugated-Cy3 or -FITC (1 : 500, Jackson Immuno Research) were used as secondary antibodies. MEF cells and SH-SY5Y cells were analyzed by immunofluorescence using either anti-flag tag (1 : 200, Sigma) or anti-Ub (1 : 100, Sigma) as the primary antibodies. Ultrastrucal studies by electron microscopy were performed as described using sciatic nerve (11).

Quantitative RT–PCR analysis and dual luciferase assays

Primers for the mouse *Uch l3* and four ubiquitin genes were designed and comparative reverse transcription–PCR (RT–PCR) was performed using Taq Man probe with the ABI PRISM 7700 (Applied Biosystems) using total RNA from wild-type and *gad* mouse brain ($n = 3$). The dual luciferase assay was performed using the +18 to +1227 bp region of the human Ub C promoter generated from human genomic DNA as per the manufacturer's instructions (Promega).

Pulse chase analysis

Transfected MEF cells were washed and incubated with methionine-free medium for 1 h. The cells were then pulsed with 200 µCi/ml [^{35}S]-Met (NEN) for 1 h and then washed and chased with 30 mM methionine for 30 h. At 0, 2, 8, 20 and 30 h the cells were harvested for immunoprecipitation with anti-Ub. Following SDS–PAGE on a 15% gel, radioactive bands were detected using the image analysis software PD QUEST (BioRad).

Transgenic UCH L1 mouse

Flag tagged mouse UCH L1 was subcloned into pEF-Bos vector under the strong promoter EF-1α. This plasmid was linearized by digestion with *Hind*III/*Aat*II, gel-purified and extracted twice with phenol/chloroform. A 2 µg/ml solution of linearized plasmid was used for pronuclear microinjection. Offspring were screened for the presence of the transgene by PCR of tail DNA. Expression of transgenic *Uch l1* mRNA was confirmed by reverse transcription of total RNA (5 µg) and subsequent PCR using specific primers (Fig. 5A). Primers to β-actin were used for internal controls.

Molecular simulation

Mouse UCH L1 was automatically modeled using Modeler software with Insight (MSI) interface. Briefly, mouse UCH L1 was modeled after the data from the crystal structure of human UCH L3 using the ClustralW algorithm. Human UCH L3 was used to derive spatial restraints expressed as probability density functions (14). These functions are used to constrain C^{α}–C^{α} distances, main chain N–O distances, main chain and side chain dihedral angles, etc. The individual constraints were assembled

into a single molecular probability density function (MPDF). The three-dimensional protein model was then obtained by optimizing this MPDF. The optimization procedure itself employed a variable target function method with a conjugate gradient minimization scheme followed by an optional restrained simulated annealing molecular dynamics scheme.

Steady-state kinetics

Steady-state kinetic measurements were conducted at 25°C in assay buffer (50 mM HEPES pH 7.5, 0.5 mM EDTA, containing 0.1 mg/ml ovalbumin and 1 mM DTT). Concentrations of enzymes were 5 nM for UCH L1 and 5 mM for D30K- and C90S-UCH L1 mutants. Ubiquitin-7-amido-4-methylcoumarin (Ub-AMC; Boston Biochem, MA, USA) served as substrate at different concentrations, and AMC production was monitored continuously by fluorescence (Wallace 1420 multilabel counter, Perkin Elmer, Turk, Finland; $\lambda_{ex} = 355$ nm, $\lambda_{em} = 460$ nm). For competition/inhibition by ubiquitin, enzymes were pre-incubated with ubiquitin for 5 min at 25°C before adding substrates. Initial velocity data were used to determine values for K_m, K_i and k_{cat} from non-linear fits of the Michaelis–Menten equation with the program PRISM (GraphPad, San Diego, CA, USA).

ACKNOWLEDGEMENTS

We thank the following people for their contributions to this work: T. Kikuchi, T. Kokubo, R. Takahashi and Y. Imai for helpful discussions; S.-M. Tilghman for kind gift of *Uch l3*$^{\Delta 3\text{-}7}$ mouse; T. Kikuchi for technical assistance with tissue sections; A. Kanou for modeling (Ryoka Systems Inc.); K. Arimoto and J. Ando for TOF MASS analysis (Applied Biosystems); F. Melandri (Boston Biochem) for advice regarding steady-state kinetic measurements; S. Kohsaka for providing SH-SY5Y cells; and M. Shikama for the care and breeding of animals. This work was supported by grants-in-aid from the Ministry of Health, Labor and Welfare of Japan, grants-in-aid for scientific research from the Ministry of Education, Culture, Sports, Science and Technology of Japan, a grant from the Organization for Pharmaceutical Safety and Research, and a grant from Japan Science and Technology Cooperation. S.A. is a fellow of the Japan Society for the Promotion of Science (JSPS). Y.-L.W. is a fellow of the Japan Foundation for Aging and Health.

REFERENCES

1. Weissman, A.M. (2001) Themes and variations on ubiquitylation. *Nat. Rev. Mol. Cell. Biol.*, **2**, 169–178.
2. Tran, P.B. and Miller, R.J. (1999) Aggregates in neurodegenerative disease: crowds and power? *Trends Neurosci.*, **22**, 194–197.
3. Wilkinson, K.D., Laleli-Sahin, E., Urbauer, J., Larsen, C.N., Shih, G.H., Haas, A.L., Walsh, S.T. and Wand, A.J. (1999) The binding site for UCH-L3 on ubiquitin: mutagenesis and NMR studies on the complex between ubiquitin and UCH-L3. *J. Mol. Biol.*, **291**, 1067–1077.
4. Larsen, C.N., Krantz, B.A. and Wilkinson, K.D. (1998) Substrate specificity of deubiquitinating enzymes: ubiquitin C-terminal hydrolases. *Biochemistry*, **37**, 3358–3368.
5. Finley, D., Bartel, B. and Varshavsky, A. (1989) The tails of ubiquitin precursors are ribosomal proteins whose fusion to ubiquitin facilitates ribosome biogenesis. *Nature*, **338**, 394–401.
6. Wilkinson, K.D., Lee, K.M., Deshpande, S., Duerksen-Hughes, P., Boss, J.M. and Pohl, J. (1989) The neuron-specific protein PGP 9.5 is a ubiquitin carboxyl-terminal hydrolase. *Science*, **246**, 670–673.
7. Wilkinson, K.D., Deshpande, S. and Larsen, C.N. (1992) Comparisons of neuronal (PGP 9.5) and non-neuronal ubiquitin C-terminal hydrolases. *Biochem. Soc. Trans.*, **20**, 631–637.
8. Lowe, J., McDermott, H., Landon, M., Mayer, R.J. and Wilkinson, K.D. (1990) Ubiquitin carboxyl-terminal hydrolase (PGP 9.5) is selectively present in ubiquitinated inclusion bodies characteristic of human neurodegenerative diseases. *J. Pathol.*, **161**, 153–160.
9. Leroy, E., Boyer, R., Auburger, G., Leube, B., Ulm, G., Mezey, E., Harta, G., Brownstein, M.J., Jonnalagada, S., Chernova, T. *et al.* (1998) The ubiquitin pathway in Parkinson's disease. *Nature*, **395**, 451–452.
10. Saigoh, K., Wang, Y.L., Suh, J.G., Yamanishi, T., Sakai, Y., Kiyosawa, H., Harada, T., Ichihara, N., Wakana, S., Kikuchi, T. *et al.* (1999) Intragenic deletion in the gene encoding ubiquitin carboxy-terminal hydrolase in *gad* mice. *Nat. Genet.*, **23**, 47–51.
11. Kikuchi, T., Mukoyama, M., Yamazaki, K. and Moriya, H. (1990) Axonal degeneration of ascending sensory neurons in gracile axonal dystrophy mutant mouse. *Acta. Neuropathol. (Berl.)*, **80**, 145–151.
12. Wilkinson, K.D. (1997) Regulation of ubiquitin-dependent processes by deubiquitinating enzymes. *FASEB J.*, **11**, 1245–1256.
13. Liu, Y., Fallon, L., Lashuel, H.A., Liu, Z. and Lansbury, P.T. (2002) The UCH-L1 gene encodes two opposing enzymatic activities that affect alpha-synuclein degradation and Parkinson's disease susceptibility. *Cell*, **111**, 209–218.
14. Johnston, S.C., Larsen, C.N., Cook, W.J., Wilkinson, K.D. and Hill, C.P. (1997) Crystal structure of a deubiquitinating enzyme (human UCH-L3) at 1.8 Å resolution. *EMBO J.*, **16**, 3787–3796.
15. Morimoto, T., Ide, T., Ihara, Y., Tamura, A. and Kirino, T. (1996) Transient ischemia depletes free ubiquitin in the gerbil hippocampal CA1 neurons. *Am. J. Pathol.*, **148**, 249–257.
16. Takada, K., Hibi, N., Tsukada, Y., Shibasaki, T. and Ohkawa, K. (1996) Ability of ubiquitin radioimmunoassay to discriminate between mono-ubiquitin and multi-ubiquitin chains. *Biochim. Biophys. Acta*, **1290**, 282–288.
17. Fujimuro, M., Sawada, H. and Yokosawa, H. (1994) Production and characterization of monoclonal antibodies specific to multi-ubiquitin chains of polyubiquitinated proteins. *FEBS Lett.*, **349**, 173–180.
18. Takada, K., Nasu, H., Hibi, N., Tsukada, Y., Ohkawa, K., Fujimuro, M., Sawada, H. and Yokosawa, H. (1995) Immunoassay for the quantification of intracellular multi-ubiquitin chains. *Eur. J. Biochem.*, **233**, 42– 47.
19. Swaminathan, S., Amerik, A.Y. and Hochstrasser, M. (1999) The Doa4 deubiquitinating enzyme is required for ubiquitin homeostasis in yeast. *Mol. Biol. Cell*, **10**, 2583–2594.
20. Amerik, A.Y., Nowak, J., Swaminathan, S. and Hochstrasser, M. (2000) The Doa4 deubiquitinating enzyme is functionally linked to the vacuolar protein-sorting and endocytic pathways. *Mol. Biol. Cell*, **11**, 3365–3380.
21. Johnston, S.C., Riddle, S.M., Cohen, R.E. and Hill, C.P. (1999) Structural basis for the specificity of ubiquitin C-terminal hydrolases. *EMBO J.*, **18**, 3877–3887.
22. Shih, S.C., Sloper-Mould, K.E. and Hicke, L. (2000) Monoubiquitin carries a novel internalization signal that is appended to activated receptors. *EMBO J.*, **19**, 187–198.
23. Nakatsu, F., Sakuma, M., Matsuo, Y., Arase, H., Yamasaki, S., Nakamura, N., Saito, T. and Ohno, H. (2000) A di-leucine signal in the ubiquitin moiety. Possible involvement in ubiquitination-mediated endocytosis. *J. Biol. Chem.*, **275**, 26213–26219.
24. Bennett, M.C., Bishop, J.F., Leng, Y., Chock, P.B., Chase, T.N. and Mouradian, M.M. (1999) Degradation of alpha-synuclein by proteasome. *J. Biol. Chem.*, **274**, 33855–33858.
25. Rochet, J.C. and Lansbury, P.T. Jr (2000) Amyloid fibrillogenesis: themes and variations. *Curr. Opin. Struct. Biol.*, **10**, 60–68.
26. Shimura, H., Hattori, N., Kubo, S., Mizuno, Y., Asakawa, S., Minoshima, S., Shimizu, N., Iwai, K., Chiba, T., Tanaka, K. *et al.* (2000) Familial Parkinson disease gene product, parkin, is a ubiquitin-protein ligase. *Nat. Genet.*, **25**, 302–305.
27. Imai, Y., Soda, M., Inoue, H., Hattori, N., Mizuno, Y. and Takahashi, R. (2001) An unfolded putative transmembrane polypeptide, which can lead to endoplasmic reticulum stress, is a substrate of Parkin. *Cell*, **105**, 891–902.

28. Bizzi, A., Schaetzle, B., Patton, A., Gambetti, P. and Autilio-Gambetti, L. (1991) Axonal transport of two major components of the ubiquitin system: free ubiquitin and ubiquitin carboxyl-terminal hydrolase PGP 9.5. *Brain Res.*, **548**, 292–299.
29. Momose, Y., Murata, M., Kobayashi, K., Tachikawa, M., Nakabayashi, Y., Kanazawa, I. and Toda, T. (2002) Association studies of multiple candidate genes for Parkinson's disease using single nucleotide polymorphisms. *Ann. Neurol.*, **51**, 133–136.
30. Satoh, J. and Kuroda, Y. (2001) A polymorphic variation of serine to tyrosine at codon 18 in the ubiquitin C-terminal hydrolase-L1 gene is associated with a reduced risk of sporadic Parkinson's disease in a Japanese population. *J. Neurol. Sci.*, **189**, 113–117.
31. Wang, J., Zhao, C.Y., Si, Y.M., Liu, Z.L., Chen, B. and Yu, L. (2002) ACT and UCH-L1 polymorphisms in Parkinson's disease and age of onset. *Mov. Disord.*, **17**, 767–771.
32. Maraganore, D.M., Farrer, M.J., Hardy, J.A., Lincoln, S.J., McDonnell, S.K. and Rocca, W.A. (1999) Case-control study of the ubiquitin carboxy-terminal hydrolase L1 gene in Parkinson's disease. *Neurology*, **53**, 1858–1860.
33. Polymeropoulos, M.H., Lavedan, C., Leroy, E., Ide, S.E., Dehejia, A., Dutra, A., Pike, B., Root, H., Rubenstein, J., Boyer, R. *et al.* (1997) Mutation in the alpha-synuclein gene identified in families with Parkinson's disease. *Science*, **276**, 2045–2047.
34. Kitada, T., Asakawa, S., Hattori, N., Matsumine, H., Yamamura, Y., Minoshima, S., Yokochi, M., Mizuno, Y. and Shimizu, N. (1998) Mutations in the parkin gene cause autosomal recessive juvenile parkinsonism. *Nature*, **392**, 605–608.
35. Bonifati, V., Rizzu, P., Van Baren, M.J., Schaap, O., Breedveld, G.J., Krieger, E., Dekker, M.C., Squitieri, F., Ibanez, P., Joosse, M. *et al.* (2002) Mutations in the DJ-1 gene associated with autosomal recessive early-onset Parkinsonism. *Science.* Published online 21 November 2002; 10.1126/science.1077209.
36. Shimura, H., Schlossmacher, M.G., Hattori, N., Frosch, M.P., Trockenbacher, A., Schneider, R., Mizuno, Y., Kosik, K.S. and Selkoe, D.J. (2001) Ubiquitination of a new form of alpha-synuclein by parkin from human brain: implications for Parkinson's disease. *Science*, **293**, 263–269.
37. Abeliovich, A., Schmitz, Y., Farinas, I., Choi-Lundberg, D., Ho, W.H., Castillo, P.E., Shinsky, N., Verdugo, J.M., Armanini, M., Ryan, A. *et al.* (2000) Mice lacking alpha-synuclein display functional deficits in the nigrostriatal dopamine system. *Neuron*, **25**, 239–252.
38. Kurihara, L.J., Semenova, E., Levorse, J.M. and Tilghman, S.M. (2000) Expression and functional analysis of Uch-L3 during mouse development. *Mol. Cell. Biol.*, **20**, 2498–2504.

Exp. Anim. 52(4), 365–369, 2003

—Note—

Immunohistochemical Analysis of Protein Gene Product 9.5, a Ubiquitin Carboxyl-terminal Hydrolase, during Placental and Embryonic Development in the Mouse

Satoshi SEKIGUCHI[1, *], Yasuhiro YOSHIKAWA[2], Satoshi TANAKA[3], Jungkee KWON[2], Yoshiyuki ISHII[2], Shigeru KYUWA[2], Keiji WADA[4], Shinichirou NAKAMURA[1], and Kimimasa TAKAHASHI[1]

[1]*Department of Veterinary Pathology, Nippon Veterinary and Animal Science University, 1–7–1, Kyounan-cho, Musashino, Tokyo 180-8602,* [2]*Department of Biomedical Science and* [3]*Cellular Biochemistry, Graduate School of Agricultural and Life Sciences, The University of Tokyo, 1–1–1 Yayoi, Bunkyo-ku, Tokyo 113-8657,* [4]*Department of Degenerative Neurological Diseases, National Institute of Neuroscience, National Center of Neurology and Psychiatry, Kodaira, Tokyo, 187-8502, *Present address: Department of Biomedical Science, The University of Tokyo, 1–1–1 Yayoi, Bunkyo-ku, Tokyo 113-8657, Japan*

Abstract: *Protein gene product 9.5 (PGP9.5) is expressed at high level in the neural and neuroendocrine systems. We investigated the localization and degree of expression of PGP9.5 in the developing mouse placenta and embryo at 6.5, 10.5 and 14 days of gestation using an immunohistochemical technique. At 6.5 days of gestation PGP9.5 was detected at various levels in decidual and primary trophoblast giant cells in the placenta, and in embryonic ectodermal cells in the embryo. At 10.5 and 14 days of gestation PGP9.5 was expressed at moderate to strong levels in neurons in the embryo, but rarely in the placenta. These findings suggest that the protein may play a significant role in implantation and placental development, and differentiation of embryonic ectoderm.*

Key words: *embryo, mouse, PGP9.5, placenta*

The ubiquitin-proteasome system is a major pathway for selective protein degradation [4]. Ubiquitin attaches to the target proteins and forms a polyubiquitin chain, and the ubiquitinated proteins are recognized and degraded by a multi-subunit protease complex, called the proteasome [1]. Ubiquitin carboxyl-terminal hydrolases recycle ubiquitin from ubiquitin/protein complexes or polyubiquitin chains by cleaving the amide linkage neighbouring the C-terminal glycine of ubiquitin [19, 20]. The protein gene product 9.5 (PGP9.5) is equivalent to ubiquitin carboxyl-terminal hydrolase isozyme L1 (UCHL1) [21]. PGP9.5 is one of the major proteins in the brain, constituting 1 to 5% of total soluble brain proteins [21]. Neuroaxonal dystrophy in the gracile nucleus of the medulla and gracile fascicules of the spinal cord occurs in the gracile axonal dystrophy (Gad) mouse due to deficiency of UCHL1 [13, 23]. The Gad mouse also exhibits deterioration of spermatogenesis with aging because PGP9.5/UCHL1 expression is defective in the spermatogonia and Sertoli cells [9].

(Received 7 February 2003 / Accepted 7 April 2003)

Address corresponding: S. Sekiguchi, Department of Biomedical Science, The University of Tokyo, 1–1–1 Yayoi, Bunkyo-ku, Tokyo 113-8657, Japan

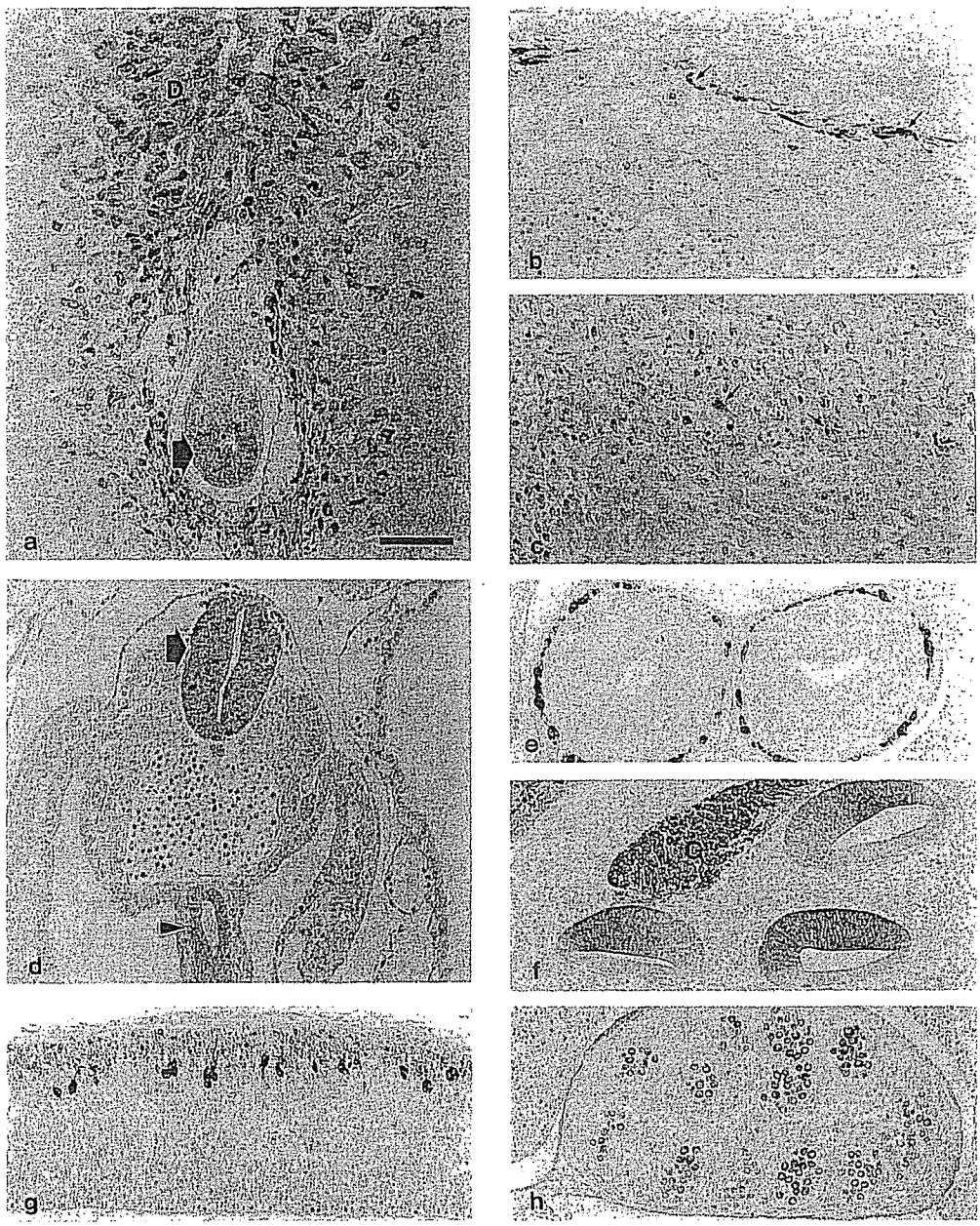

Fig. 1. Immunohistochemical reaction of PGP9.5. Hematoxylin counterstained, Bar = 100 μm. In placenta, PGP9.5 is detected at various levels in decidual cells (D) around the embryo at 6.5 days of gestation (a); in decidual cells (arrows) in the small area of basal decidua at 10.5 days of gestation (b); and at 14 days of gestation (c). In the embryo, PGP9.5 is detected at various levels in embryonic ectodermal cells (arrow in Fig. a) at 6.5 days of gestation; in most of neural tubular cells (arrow) and intestinal epithelial cells (arrow head) at 10.5 days of gestation (d); in neurons of the peripheral nervous system (e); in neurons of the ganglion (G) and epithelial cells of semicircular canals (f); migrated mature neurons of the mesencephalon (g); and in gonocytes of the testis at 14 days of gestation (h).

Immunohistochemical studies have demonstrated that PGP9.5 is highly expressed in neuronal and neuroendocrine tissues [3, 6, 10, 15, 24, 25], and PGP9.5 has also been shown to be expressed in the distal tubular epithelial cells, ova and corpus luteum cells of the ovary, Leydig cells and Sertoli cells of the testis of the mouse [8, 22], synoviocytes in the joints of the horse [7], and hair follicle cells of the rat [11]. Localization of PGP9.5

in the mouse embryo has also been described [6, 14]. PGP9.5 is present at high levels in the neuronal tissues in mouse embryo after 10.5 days of gestation [19], and in rat embryos after 11.5 days of gestation [6]. Though the presence of this protein has been revealed in the embryo, little is known about the placenta. The placenta fulfills indispensable functions such as metabolism, and provides an immunological barrier and endocrine secretion for embryonic development. In this paper we examined the localization and degree of the expression of PGP9.5 in the mouse placenta and embryo during the period of pregnancy.

C57BL/6J mice of both sexes were allowed to mate and midday when a vaginal plug was recognized was considered as day 0.5 of gestation. Two female mice at 6.5, 10.5 and 14 days of gestation, respectively, were sacrificed by cervical dislocation under ether anesthetization. Embryos and whole uterus were fixed in Bouin's solution for 5 to 6 h, then embedded in paraffin. Paraffin sections were cut at 5 to 6 μm in thickness, deparaffinized in xylene, and stained with haematoxylin and eosin.

Immunostaining was carried out by a labeled streptavidin-biotin (LsAB) method using rabbit anti-human PGP9.5 polyclonal antibody (Ultraclone Ltd. U.K.) as a primary antibody. Deparaffinized sections were pretreated with 0.3% H_2O_2 in methanol for 30 min and washed in phosphate buffer saline (PBS). In order to enhance immunoreactivity, sections were subjected to autoclave treatment for 10 min at 121°C. Non-specific binding of immunogloblins was blocked by incubation with Block Ace (Dainippon pharamaceutical Ltd. Japan) for 1 h at room temperature. After blocking, sections were incubated with primary antibody diluted at 1 : 8000 for 16 h at 4°C. Next, sections were incubated with biotinylated goat anti-rabbit IgG (DAKO Ltd. Denmark) diluted at 1 : 500 for 30 min at 37°C, and after washing in PBS, they were reacted with horseradish peroxidase conjugated streptavidin (DAKO Ltd. Denmark) diluted at 1 : 500 for 30 min at room temperature. After washing in PBS, the immunoreaction was visualized by incubation in 3,3'-diaminobenzidine tetrahydrochloride (DAB)-H_2O_2 solution and then counterstained with haematoxylin. Negative control sections were incubated with PBS or non-immunized rabbit serum as substitutes for the primary antibody. Taking into consideration which stage and what kind of cell expresses PGP9.5, the intensities of immunoreactions were classified into one of three grades: weak, moderate or strong.

The immunoreactivity of PGP9.5 was detected at various levels in decidual cells around the embryo and in primary trophoblastic giant cells at 6.5 days of gestation (Fig. 1a). The moderately or strongly positive decidual cells showed not only cytoplasmic but also nuclear staining. At 10.5 days of gestation, decidual cells with various levels of staining were seen in the smaller area of the basal decidua, and they also showed nuclear staining (Fig. 1b). At 14 days of gestation, a few cells stained positive at weak to moderate levels were present in the basal decidua (Fig. 1c , Table1). There was no difference in immunoreactivity of PGP9.5 among mouse placentas of the same litter mates.

At 6.5 days of gestation, moderate PGP9.5 immunoreactivity was detected in embryonic ectodermal cells (Fig. 1a). At 10.5 days of gestation, most neural tubular cells and intestinal epithelial cells were immunopositive at a moderate grade (Fig. 1d). In addition, otic vesicular cells, epithelial cells of the Wolffian duct, and notocord cells were weakly immunopositive. At 14 days of gestation, most of neurons were moderately or strongly positive. The neurons of the peripheral

Table 1. PGP9.5-positive cells in placenta of pregnant mouse

Grade	6.5 days	10.5 days	14 days
+	Decidual cells Primary trophoblastic giant cells	Basal decidual cells	Basal decidual cells
++	Decidual cells Primary trophoblastic giant cells	Basal decidual cells	Basal decidual cells
+++	Decidual cells	Basal decidual cells	

PGP9.5-positive reaction was classified into three grades: weak (+), moderate (++) and strong (+++). 6.5, 10.5 and 14 days mean gestation period.

Table 2. PGP9.5-positive cells in embryo of pregnant mouse

Grade	6.5 days	10.5 days	14 days
+		Neural tubular cells Otic vesicular cells Wolffian ductal cells Notocord cells Intestinal epithelial cells	Ependymocytes Adenohypophysis cells Epithelial cells of nasal pit bronchi mesonephric duct mesonephric tubule paramesonephric duct ureter hair follicle Gonocytes of testis Chondroblasts
++	Embryonic ectodermal cells	Neural tubular cells Intestinal epithelial cells	Neurons of central nervous system Gonocytes of testis
+++			Neurons of central and peripheral nervous system Epithelial cells of retina and semicircular canals

PGP9.5-positive reaction was classified into three grades: weak (+), moderate (++) and strong (+++). 6.5, 10.5 and 14 days mean gestation period.

nervous system (Fig. 1e), ganglions (Fig. 1f), migrated mature neurons of the mesencephalon (Fig. 1g), and sensory epithelial cells of the retina and semicircular canals (Fig. 1f) were especially strongly stained. These strongly immunopositive cells also showed nuclear staining. Moreover, gonocytes of testis (Fig. 1h) were weakly or moderately stained, and a weak, positive reaction was seen in ependymocytes, adenohypophysis cells, epithelial cells of nasal pit, bronchi, mesonephric duct, mesonephric tubule, paramesonephric duct, ureter, hair follicle and some chondroblasts (Table 2). PGP9.5 expression in the embryo changed with embryogenesis, however, there was no difference in the immunoreactivity of PGP9.5 of mouse embryos among the same litter mates.

This study showed that PGP9.5 was expressed at various levels in decidual cells from the early stage of pregnancy, while the number of PGP9.5 positive cells decreased in the late stage. Generally, after implantation, the area occupied by decidual cells increases from 6 days to 10 days of gestation, and thereafter slightly decreases in the mouse [5]. The structure of the mouse placenta was unchanged after 14 days of gestation [17], and its weight and the number of the constituent cells reached a plateau by 14 days of gestation [5]. In fact, the decidual cells expressing PGP9.5 appeared and increased immediately after implantation, and thereafter most of them had disappeared by the time the placenta matured.

At 6.5 days primary trophoblastic giant cells were immunopositive at low to moderate levels, whereas at 10.5 and 14 days trophoblastic giant cells were all negative. Primary trophoblastic giant cells are derived from embryonal trophoblast and invade the maternal tissue on implantation [17]. This early expression of PGP9.5 in decidual and primary trophoblastic giant cells and the subsequent decreasing number of the positive cells suggest that the protein may play a significant role in implantation and placenta development Decidual cells are thought to function as a barrier to prevent immune rejection between the maternal body and embryo [18]. Therefore, they might degrade immunoproteins which are disadvantageous for embryo development.

In the embryo of the pregnant mouse PGP9.5 was already been expressed at a moderate level in embryonic ectodermal cells at 6.5 days of gestation, and the protein was expressed at moderate to strong levels in mature neurons at 10.5 and 14 days of gestation. The

nerves develop from the embryonic ectoderm [12]. This means that the protein plays an important role in degradation of unnecessary proteins in the process of embryonic ectodermal differentiation. Mature neurons expressed the protein more strongly than immature ones; therefore, we assume that the more neurons mature, the more active their metabolism becomes. This assumption is supported by the immunostaning of PGP9.5 in the nucleus as well as the cytoplasm in mature neurons.

At 10.5 days and 14 days of gestation PGP9.5 was demonstrated at low to moderate leves in the endodermal and mesodermal tissues, such as testis and bronchi. Although the distribution of PGP9.5 mRNA in developing gonads in the mouse was reported by Schofield *et al.* [14], this is the first description of the expression of PGP9.5 protein in the developing mouse embryo. The distribution of the protein in the developing lung was reported in human and rat [2, 16]. The significance of the expressions of PGP9.5 in the developing embryo remains unclear.

References

1. Cooper, G.M. 2000. The cell, 2nd ed., The American Society for Microbiology, Washington D. C.
2. Haley, K.J., Drazen, J.M., and Osathanondh, R. 1997. Comparison of the ontogeny of protein gene product 9.5, chromogranin A and proliferating cell nuclear antigen in developing human lung. *Microsc. Res. Techniq.* 37: 62–68.
3. Hamzeh, H., Gaudillere, A., and Sabido, O. 2000. Expression of PGP9.5 on Langerhans' cells and their precursors. *Acta. Derm. Venereol.* 80: 14–16.
4. Hershko, A. and Ciechanover, A. 1992. The ubiquitin system for protein degradation. *Annu. Rev. Biochem.* 61: 761–807.
5. Iguchi, T., Tani, N., Sato, T., Fukatsu, N., and Ohta, Y. 1993. Development change in placenta cells from several stage of pregnancy *in vivo* and *vitro*. *Biol. Reprod.* 48: 188–196.
6. Kent, C. and Clarke, P.J. 1991. The immunolocalisation of the neuroendocrine specific protein PGP9.5 during neurogenesis in the rat. *Dev. Brain Res.* 58: 147–150.
7. Kitamura, H.P., Yanase, H., Kitamura, H., and Iwanaga, T. 1999. Unique localization of protein gene product 9.5 in type B synoviocytes in the joints of the horse. *J. Histochem. Cytochem.* 47: 343–351.
8. Kon, Y., Endoh, D., and Iwanaga, T. 1999. Expression of protein gene product 9.5, a neuronal ubiquitin C-terminal hydrolase, and its developing change in Sertoli cells of mouse testis. *Mol. Reprod. Dev.* 54: 333–341.
9. Kwon, J., Kikuchi, T., Setsuie, R., Ishii, Y., Kyuwa, S., and Yoshikawa Y. 2003. Characterization of the testis in congenitally ubiquitin carboxy-terminal hydrolase-1 (Uch-L1) defective (gad) mice. *Exp. Anim.* 52: 1–9.
10. Leibl, M.A., Ota, T., WoodWard, M.N., Kenny, S.E., Lloyd, D.A., Vaillant, C.R., and Edgar, D.H. 1999. Expression of endothelin 3 by mesenchymal cells of embryonic mouse caecum. *Gut.* 44: 246–252.
11. Ohsawa, T. 2001. Neuron-specific PGP9.5 expression in rat hair follicle development and cycle. *J. Dermatol. Sci.* 26: 100–105.
12. Patten, B.M. and Carlson, B.M. Foundation of embryology 3rd ed., McGraw-Hill, New York.
13. Saigoh. K., Wang, Y., and Suh, J. 1999. Intragenic deletion in the gene encoding ubiquitin carboxy-terminal hydrolase in gad mice. *Nat. Genet.* 23: 47–51.
14. Schofield, J.N., Day, I.N.M., Thompson, R.J., and Edwards, Y.H. 1995. PGP9.5, a ubiquitin C-terminal hydrolase;patern of mRNA and protein expression during neural development in the mouse. *Dev. Brain Res.* 85: 229–238.
15. Sidebotham, E.L., Woodwar, M.N., Kenny, S.E., Lloyd, D.A., Vaillant, C.R., and Edgar, D.H. 2001. Assessment of protein gene product 9.5 as a marker of neural crest-derived precursor cells in the developing enteric nervous system. *Pediatr. Surg. Int.* 17: 304–307.
16. Sorokin, S.P., Ebina, M., and Hoyt, R.F. 1993. Development of PGP9.5 and calcitonin gene-related peptide-like immunoreactivity in organ cultured fetal rat lungs. *Anat. Res.* 236: 213–225.
17. Theiler, K. 1989. The house mouse, Springer-Verlag, New York.
18. Green, L.E. 1996. Biology of the laboratory mouse, 2nd ed., Doer Publications, New York.
19. Wilkinson, K.D. 1995. Roles of ubiquitinylation in proteolysis and cellular reguletion. *Annu. Rev. Nutr.* 15: 161–189.
20. Wilkinson, K.D., Deshpande, S., and Larsen, C.N. 1992. Comparisons of neural (PGP9.5) and non-neuronal ubiquitin C-terminal hydrolases. *Biochem. Soc. T.* 20: 631–637.
21. Wilkinson, K.D., Lee, K., Deshpande, S., Duerksen-Hughes, P., Boss, J.M., and Pohl, Jan. 1989. The neuron-specific protein PGP9.5 is a ubiquitin carboxyl-terminal hydrolase. *Science.* 246: 670–673.
22. Wilson, P.O.G., Barber, P.C., Hamid, Q.A., Power, B.F., Dhillon, A.P., Rode, J., Day, I.N.M., Thompson, R.J., and Polak, J.M. 1988. The immunolocalisation of Protein gene product 9.5 using rabbit polyclonal and mouse monoclonal antibodies. *Br. J. Exp. Pathol.* 69: 91–104.
23. Yamazaki, K., Wakasugi, N., Tomita, T., Kikuchi, T., Mokuyama, M., and Ando, K. 1988. Gracile axonal dystrophy (GAD), a new neurological mutant in mouse. *Proc. Soc. Exp. Bio. Med.* 187: 209–215.
24. Yang, P., Hirose, T., Hasegawa, T., Seki, K., Nakanishi, H., and Hizawa, K. 1996. Ultrastructual heterogeneity of acquired intradermal melanocytic nervus cells. *Ultrastruct. Pathol.* 20: 255–261.
25. Young, H.M. 1999. Embryological origin of interstitial cells of Cajal. *Microsc. Res. Techniq.* 47: 303–308.

Biophysical Journal Volume 85 August 2003 1176–1185

Molecular Dynamics Simulation of Dimeric and Monomeric Forms of Human Prion Protein: Insight into Dynamics and Properties

Masakazu Sekijima,* Chie Motono,* Satoshi Yamasaki,† Kiyotoshi Kaneko,‡ and Yutaka Akiyama*

*Computational Biology Research Center, National Institute of Advanced Industrial Science and Technology, 2-41-6 Aomi, Koto-ku, Tokyo 135-0064, Japan; †Department of Biotechnology, University of Tokyo, 1-1-1 Yayoi, Bunkyo-ku, Tokyo 113-8657, Japan; and ‡Department of Cortical Function Disorders, National Institute of Neuroscience, National Center of Neurology and Psychiatry and Japan Science and Technology Corporation, 4-1-1 Ogawa-Higashi, Kodaira, Tokyo 187-8502, Japan

ABSTRACT A central theme in prion protein research is the detection of the process that underlies the conformational transition from the normal cellular prion form (PrP^C) to its pathogenic isoform (PrP^{Sc}). Although the three-dimensional structures of monomeric and dimeric human prion protein (HuPrP) have been revealed by NMR spectroscopy and x-ray crystallography, the process underlying the conformational change from PrP^C to PrP^{Sc} and the dynamics and functions of PrP^C remain unknown. The dimeric form is thought to play an important role in the conformational transition. In this study, we performed molecular dynamics (MD) simulations on monomeric and dimeric HuPrP at 300 K and 500 K for 10 ns to investigate the differences in the properties of the monomer and the dimer from the perspective of dynamic and structural behaviors. Simulations were also undertaken with Asp178Asn and acidic pH, which is known as a disease-associated factor. Our results indicate that the dynamics of the dimer and monomer were similar (e.g., denaturation of helices and elongation of the β-sheet). However, additional secondary structure elements formed in the dimer might result in showing the differences in dynamics and properties between the monomer and dimer (e.g., the greater retention of dimeric than monomeric tertiary structure).

INTRODUCTION

Transmissible spongiform encephalopathies are neurodegenerative diseases that are attributable to the structural transformation of cellular prion (PrP^C) to its anomalous isoform (PrP^{Sc}). In humans, these diseases include kuru, Creutzfeldt-Jakob disease, fatal familial insomnia, and Gerstmann-Sträussler-Scheinker syndrome; in sheep, scrapie; and in cattle, bovine spongiform encephalopathy. The most important aspect of prion disease is the conformational transition of PrP^C to PrP^{Sc}, both of which are isoforms with identical amino acid sequence. However, comparison of the secondary structures shows that PrP^C is ~42% helical with a very low (~3%) β-sheet content, whereas PrP^{Sc} consists of 30% α-helices and 43% β-sheets. Although the precise physiological role of PrP^C and the chemical differences between PrP^C and PrP remain unknown, it appears that the differences are conformational (Pan et al., 1993; Safar et al., 1993).

The three-dimensional structures of monomeric PrP^Cs from various sources have been determined by NMR spectroscopy (Riek et al., 1996; Donne et al., 1997; Zhang et al., 1997; Lopez et al., 2000; Zahn et al., 2000) and found to be very similar among many species. The N-terminal region (residues 23–124) is flexible, and the C-terminal region (residues 125–228) that contains the globular domains is well structured. All of these structures contain intramolecular disulfide bridges, three α-helices, and a short double-stranded β-sheet (Fig. 1 *a*). Recent x-ray crystallographic studies determined the dimeric form of human PrP^C (Knaus et al., 2001). The dimer is the result of three-dimensional swapping of the C-terminal helix 3 and rearrangement of the disulfide bonds (Fig. 1 *b*). The transition process from PrP^C to PrP^{Sc} has been explained by two popular models. According to the heterodimer model (Prusiner, 1991; Cohen et al., 1994), PrP^{Sc} induces the conformational change of PrP^C by contact. The nucleation-dependent polymerization model of Lansbury and Caughey (1995), on the other hand, suggests that PrP^{Sc} acts as a crystal seed at the starting point for crystal-like growth of a PrP^{Sc} oligomer and that conformational change occurs via transient interaction between PrP^C and PrP^{Sc}. Several mutations in the primary structure of PrP^C are known to segregate in a variety of transmissible spongiform encephalopathies (Prusiner, 1996). In this study, we selected the Asp178Asn (D178N) mutation known to be associated with fatal familial insomnia (Met^{129}/Asn^{178}). In the D178N mutation, the change from a positively charged to an uncharged residue may affect the hydrogen-bonding network and salt bridge (Riek et al., 1998). Recombinant forms of human and murine PrP^C manifest a pH-dependent conformational change in the pH range of 4.4–6, a loss of helix, and a gain of strands (Swietnicki et al., 1997; Hornemann and Glockshuber, 1998). Lower pH values accelerated conversion in a cell-free conversion assay (Kocisko et al., 1995). Thus, acidic pH may play a role in facilitating the conformational change that ultimately results in the formation of PrP^{Sc}.

More recent conformational conversion models focus on intra- and intermolecular disulfide bonds (Welker et al., 2001, 2002; Tompa et al., 2002). Some experiments have suggested that intramolecular disulfide bonds in PrP^C are required for its conversion to PrP^{Sc} (Muramoto et al., 1996;

Submitted September 26, 2002, and accepted for publication April 10, 2003.

Address reprint requests to Masakazu Sekijima, Tel.: +81-3-3599-8080; Fax: +81-3-3599-8081; E-mail: sekijima@cbrc.jp.

0006-3495/03/08/1176/10 $2.00

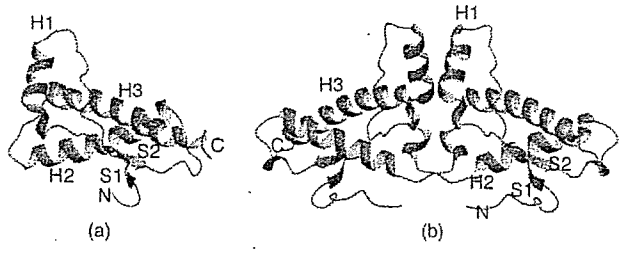

FIGURE 1 Schematic ribbon diagram of HuPrPc: (*a*) monomer; (*b*) dimer.

Herrmann and Caughey, 1998; Maiti and Surewicz, 2001). To weaken these disulfide bonds, a hypothetical molecular chaperone may be necessary (Telling et al., 1995; Kaneko et al., 1997).

Dimerization is usually required for proteins to evolve oligomeric proteins (Monod et al., 1965). With respect to PrP, Meyer et al. (2000) reported a monomer-dimer equilibrium under native conditions in a fraction of PrP^C from bovine brain (Meyer et al., 2000). Others have suggested that three-dimensional domain-swapping-dependent oligomerization is an important step in the conformational change of PrP^C to PrP^{Sc} (Knaus et al., 2001; Riley et al., 2002; Tompa et al., 2002). However, the function and dynamics of the dimeric form of PrP^C remain to be elucidated.

Molecular dynamics (MD) simulations are widely used to simulate the motion of molecules to gain a deeper understanding of the chemical reactions, fluid flow, phase transitions, and other physical phenomena due to molecular interactions (Hansson et al., 2002). Rapidly increasing computational power has made MD simulation a powerful tool for studying the structure and dynamics of biologically important molecules. Taking into account all electrostatic interactions by using the particle-mesh Ewald (PME) method, relatively long (2–3 ns) simulations with the explicit solvent water box can be carried out (Darden et al., 1993, 1999). Day et al. (2002) have shown that by increasing the temperature, protein unfolding can be accelerated without changing the pathway of unfolding, and that this method is suitable for elucidating the details of protein unfolding at minimal computational expense. With these methods, one can obtain proper trajectories that reflect the conformational and dynamic characteristics of molecules at each time point during simulation.

Most reported MD simulations of PrP^C have been reported (Zuegg and Greedy, 1999; Guilbert et al., 2000; Wong et al., 2000; Parchment and Essex, 2000; El-Bastawissy et al., 2001; Gsponer et al., 2001; Okimoto et al., 2002), involved short simulation times of <2 ns or were performed using the AMBER ff94 force field (Cornell et al., 1995), and all of the previously reported simulation targets were the monomer. Higo et al. (2001) used the multi-canonical method to show that the ff96 force field (Kollman et al., 1997) reproduces the energy landscape more correctly than does the ff94 force field both in vacuo and in solvent water. We now report the first MD simulation of the dimeric PrP^C conformation. The aim of our study was to assess differences in the functions and dynamics of the PrP monomer and dimer. We performed eight 10-ns MD simulations of PrP^C dimer and monomer using the AMBER ff96 potential under different experimental conditions: a temperature of 300 K and 500 K, D178N mutant, and acidic pH.

MATERIALS AND METHODS

All simulations were performed with the AMBER 7 program package (Case et al., 2002) using the ff96 force field. The starting structures were human cellular prion protein ($HuPrP^C$) entry 1QM2 (residues 125–228; Zahn et al., 2000) as a monomer model and 1I4M (chain A, residues 119–226; chain B: residues 227–334; Knaus et al., 2001) as a dimer model in the Brookhaven Protein Data Bank (Berman et al., 2000; Westbrook et al., 2002). We built the dimeric form of PrP^C from 1I4M using Insight II. There are disulfide bonds between Cys^{179}–Cys^{214} in the monomer and between Cys^{179}–Cys^{311} and Cys^{214}–Cys^{287} in the dimer. To establish an acidic pH environment, Asp, Glu, and His residues were protonated. The systems were surrounded with a 20-Å layer of TIP3P water molecules (Jorgensen et al., 1983) and neutralized by sodium ions using the LeaP module of AMBER 7. The number of solvent water molecules and counterions in each system are shown in Table 1. The solvated proteins with their counterions were minimized by 1000 conjugate gradient steps, heated from 0 to 300 K during 35 ps at temperature increments of 50 K every 5 ps, and kept at 300 K within 20 ps using the constant pressure and temperature algorithm (Berendsen et al., 1984). The SHAKE algorithm (Ryckaert et al., 1977) and PME algorithm with nonbonded cutoffs of 8 Å were used during heating. After equilibration, the production MD phase was carried out at 300 or 500 K for 10 ns using the constant volume and temperature ensemble and the PME algorithm with nonbonded cutoffs of 8 Å during simulation. All simulations were performed on the Magi (massively parallel computer for genome informatics) cluster running SCore 4.1 (Hori et al., 1996) at the Computational Biology Research Center. During the data-collection stage, the structures were saved to file every 250 fs. Secondary structures were analyzed using DSSP software (Kabsch and Sander, 1983), and images of simulated proteins were generated using MOLMOL software (Koradi et al., 1996).

RESULTS AND DISCUSSION

Simulation stability

Fig. 2 shows the Cα root-mean-square deviations (RMSDs) from the initial structures of globular domains of HuPrPs. In this paper, we define residues 129–223 [including strand

TABLE 1 Simulation conditions

	No. of ions	No. of water molecules
WT		
Monomer	3 Na^+	6814
Dimer	8 Na^+	9374
D178N		
Monomer	2 Na^+	6807
Dimer	6 Na^+	9373
Acidic pH		
Monomer	15 Cl	7168
Dimer	28 Cl	9714

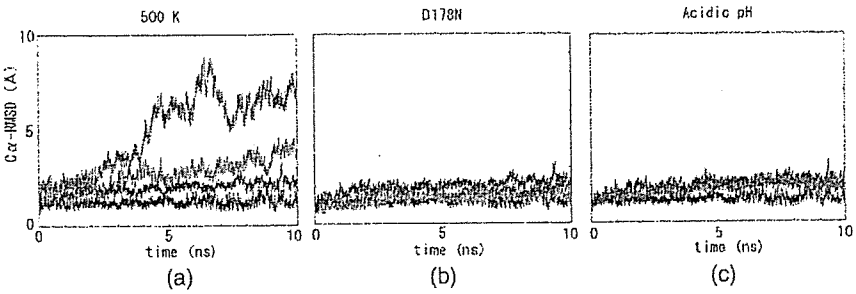

FIGURE 2 RMSD values of Cα from the initial structures. (*a–c*) Red and blue lines indicate RMSD values of the dimer and the monomer at 300 K, respectively. (*a*) Green and pink lines indicate RMSD values of the dimer and the monomer at 500 K, respectively. (*b*) Green and pink lines indicate RMSD values of the dimer and the monomer at D178N, respectively. (*c*) Green and pink lines indicate RMSD values of the dimer and the monomer at acidic pH, respectively.

1 (S1), helix 1 (H1), strand 2 (S2), helix 2 (H2), and helix 3 (H3)] of the monomer and dimer (chain A) as globular domains. As we encountered few differences in the Cα RMSD values for each dimeric subunit (data not shown), averaged data were used to present our results. In Fig. 2, *a–c*, simulation data at 300 K are shown as control data. In the simulation at 300 K, the Cα RMSD values for both the monomer and the dimer remained relatively low for a duration of 10 ns, although the monomer deviated from the initial structure more than the dimer. The average RMSD values of the monomer and dimer in the last 5 ns were 2.18 and 1.27 Å, respectively. In Fig. 2 *a*, at 500 K, the Cα RMSD values of the monomer increased and reached 9.01 Å at 6.6 ns. In contrast, the Cα RMSD values of the dimer increased gently; the peak deviation was 4.7 Å at 9.2 ns. The average RMSD values of the monomer and dimer in the last 5 ns were 6.63 Å and 3.23 Å, respectively, indicating that the monomer increased faster than the dimer. This tendency was a characteristic common to simulations at 300 K and 500 K. In Fig. 2, *b* and *c*, under conditions of D178N and acidic pH, the Cα RMSD values of both the monomer and the dimer showed the same tendency as they did at 300 K. At D178N, the peak values of Cα RMSD values were 2.76 Å and 1.32 Å, respectively. The average Cα RMSD values of the monomer and dimer in the last 5 ns were 1.72 Å and 1.44 Å, respectively, indicating that little conformation change occurred in the protein tertiary structure. At acidic pH values, the monomer and dimer peak Cα RMSD values were 2.86 Å at 4.45 ns and 2.81 Å at 9.94 ns, respectively. The average RMSD values of the monomer and dimer in the last 5 ns were 2.01 Å and 2.05 Å.

Secondary structure evolution

Figs. 3 and 4 show the secondary structure evolution during simulation as determined by the DSSP program (Kabsch and Sander, 1983). Figs. 5 and 6 are ribbon illustrations of snapshots of the trajectories. Figs. 3 *a* and 5 *a* depict simulation results of monomer HuPrP at 300 K. Although residues 152–156 of the H1 region formed a 3_{10}-helix or H-bonds over a 0.0–7.0-ns period, after 8.0 ns they formed an α-helix. Other secondary structure elements (S1, S2, H2, and H3) were retained throughout the simulation; however, several elongated S1 and S2 elements were observed until 4.0 ns (see the snapshot at 3.0 ns in Fig. 5 *c*). As shown in Figs. 3 *b* and 5 *b*, at ~2.0 ns at 500 K, the monomer began to unfold in the β-sheet and at the C-terminus of H2 and H3. It appears that the degradation of the helices corresponds with the increase in Cα RMSD observed from 2.0 to 4.0 ns (Fig. 2 *a*). We noted subsequent changes in the secondary structure at 4.0–6.0 ns: *1*), the transient formation of nonnative β-sheets at residues 129–130 and 222–223 and residues 132–133 and 159–160 and their unfolding, *2*), the unfolding of the C-terminus of H2, and *3*), the unfolding and refolding of H1 (Fig. 5 *d*). These changes produced a rapid increase in the Cα RMSD of the monomer to 7.2 Å at 4.6 ns (Fig. 2 *a*). Although the simulation at 500 K was denaturation simulation, we can consider the results as conformational search at 500 K. Fig. 5 *d* shows the denaturation state of H1 at 4.55 ns, the elongated S1 and S2 elements, and the additional β-sheet at 4.65 ns. Glockshuber et al. (1997) and Korth et al. (1997) demonstrated that the structure of H1 is different between PrP^C and PrP^{Sc} and suggested this region might form β-sheet. There were notable changes in secondary structure elements from 6.0 to 7.0 ns. There were some instances of fluctuation in the loop and the Cα RMSD value reached 9.01 Å at 6.6 ns. At 300 and 500 K, comparison with the monomer revealed that the dimer contained two additional structural elements, helices H′ (residues 194–197 and 302–305) and a β-sheet S′ (residues 191–193 and 299–301), that formed subunit interfaces (Fig. 3, *c* and *d*). At 300 K, all elements including S′ and H′ were retained throughout the simulation, although there was slight disruption at some points (see Fig. 3 *c*). The C-terminus of H1 tended to form a 3_{10}-helix. In H2, H3, and H′, there were several H-bonds. At 500 K, the C-terminus of helices crumbled like that of monomer (Fig. 3 *d*). Our results imply that in both the monomer and the dimer, there is a tendency for H1, H2, and H3 to unfold, and that they share conformational vulnerability in these regions. Although in both the monomer and dimer we noted a similar tendency for the denaturation of several regions, the dimeric form retained a remnant of the initial structure (Fig. 5 *e*). S1, S2, and S′ were retained throughout the simulation. In fact, as shown in Fig. 2 *a*, the Cα RMSD values of the dimer increased more slowly than those of the monomer. Intersubunit interactions

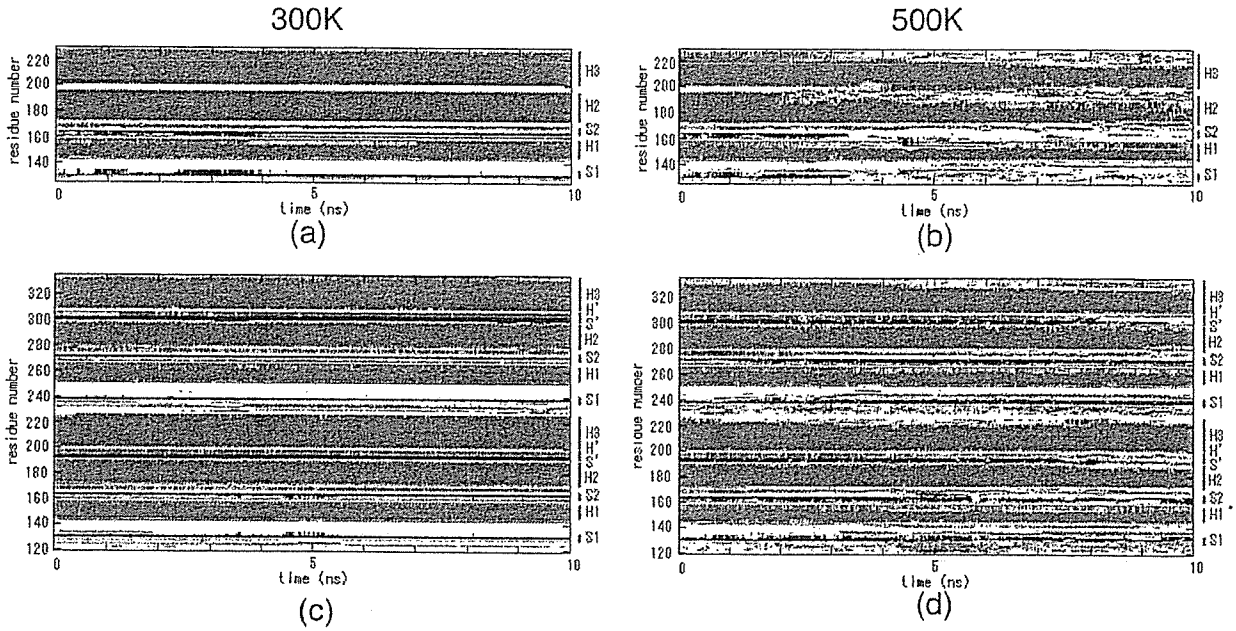

FIGURE 3 Secondary structure as a function of simulation time determined with DSSP. (*a*) Monomer at 300 K; (*b*) monomer at 500 K; (*c*) dimer at 300 K; and (*d*) dimer at 500 K. The α-helix is shown in green, the 3_{10}-helix in light green boxes, the β-strand in red boxes, the β-bridge in blue boxes, the bend in pink boxes, and the H-bond in yellow boxes.

of H′, S′, and H1 and its molecular size (weight) may contribute to solidity of the dimer.

At D178N, residues 167–169 and 275–277 (residues 167–169 in chain B) in the dimer were mainly H-bonds; however, the helices were similar to those seen at 300 K (Fig. 4, *a* and *c*). In both the monomer and dimer, we noted several elongations of β-sheets, which were more pronounced in the monomer (Fig. 4, *a* and *c*, and Fig. 6, *a* and *c*).

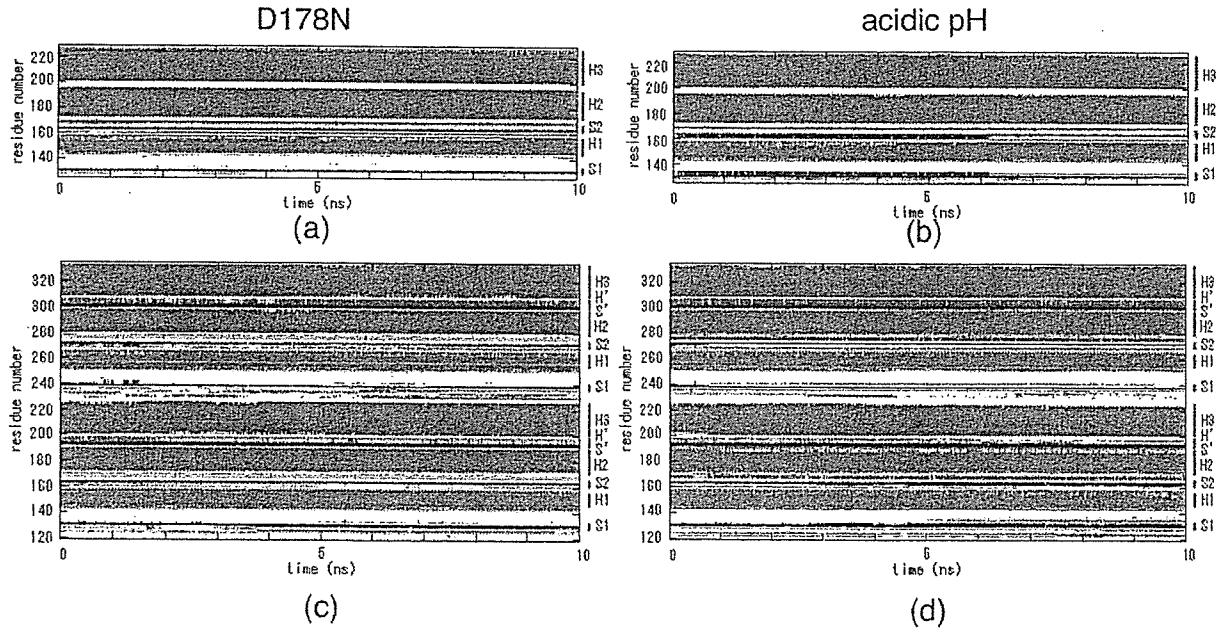

FIGURE 4 Secondary structure as a function of simulation time determined with DSSP. (*a*) Monomer at acidic pH and (*b*) dimer at acidic pH. The α-helix is shown in green, the 3_{10}-helix in light green boxes, the β-strand in red boxes, the β-bridge in blue boxes, the bend in pink boxes, and the H-bond in yellow boxes.

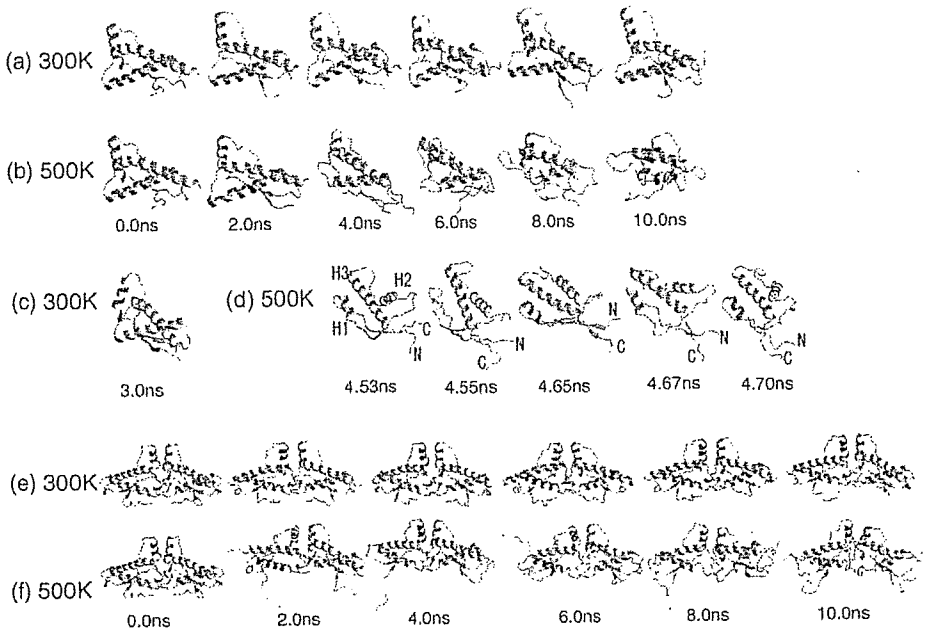

FIGURE 5 (*a*) Temporal history of the monomer at 300 K; (*b*) temporal history of the monomer at 500 K; (*c*) one snapshot of the monomer at 300 K; (*d*) details of temporal history of the monomer at 500 K around 4.6 ns; (*e*) temporal history of the dimer at 300 K; and (*f*) temporal history of the dimer at 500 K.

At acidic pH values, several H-bonds were formed at the C-terminus of H1 in the dimer; however, the helices were similar to those seen at 300 K (Fig. 4, *b* and *d*). In both the monomer and dimer, we noted several elongations of β-sheets, which were more pronounced in the monomer (Fig. 4, *b* and *d*, and Fig. 6, *b* and *d*).

Percentage of secondary structure

Fig. 7 shows the percentage (abundance ratio) of secondary structures per residue throughout the simulation. At 300 K, the α-helix, H1, and H2 were longer in the monomer than the dimer. In H1, there seemed to be a predilection for elongating to the C-terminus side (Fig. 7 *a*) and a simultaneous tendency of the C-terminus to form a 3_{10}-helix in the monomer. S1 tended to elongate to the C-terminus side whereas S2 exhibited a tendency for elongation to the N-terminus side (Fig. 5 *c*) in both the monomer and dimer. S′ remained intact throughout the simulation.

At 500 K, fewer α-helices, 3_{10}-helices, and β-sheets were formed than at 300 K (Fig. 7 *b*). Monomeric H1, H2, and H3 tended to denature more than their dimeric counterparts.

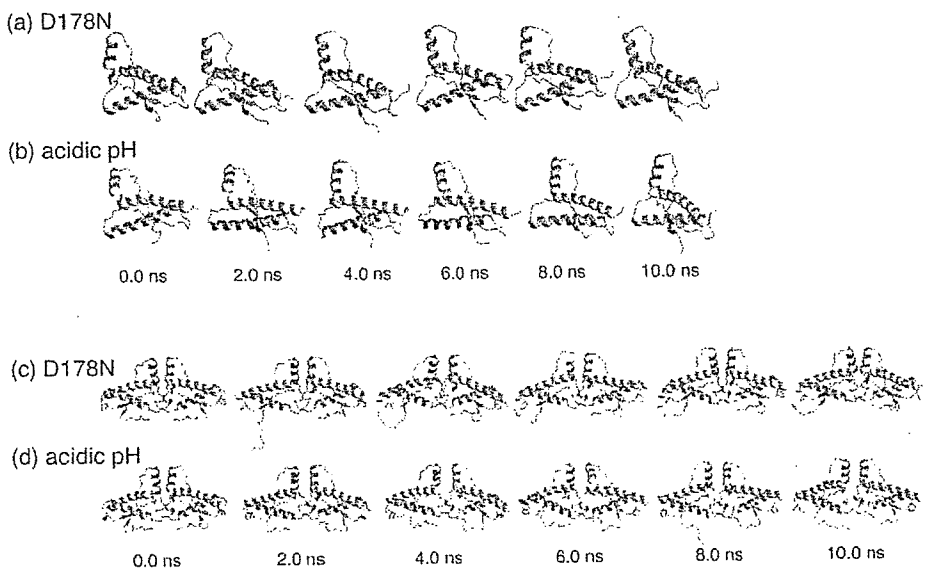

FIGURE 6 Temporal history of (*a*) the monomer at D178N; (*b*) the monomer at acidic pH; (*c*) the dimer at D178N; and (*d*) the dimer at acidic pH.

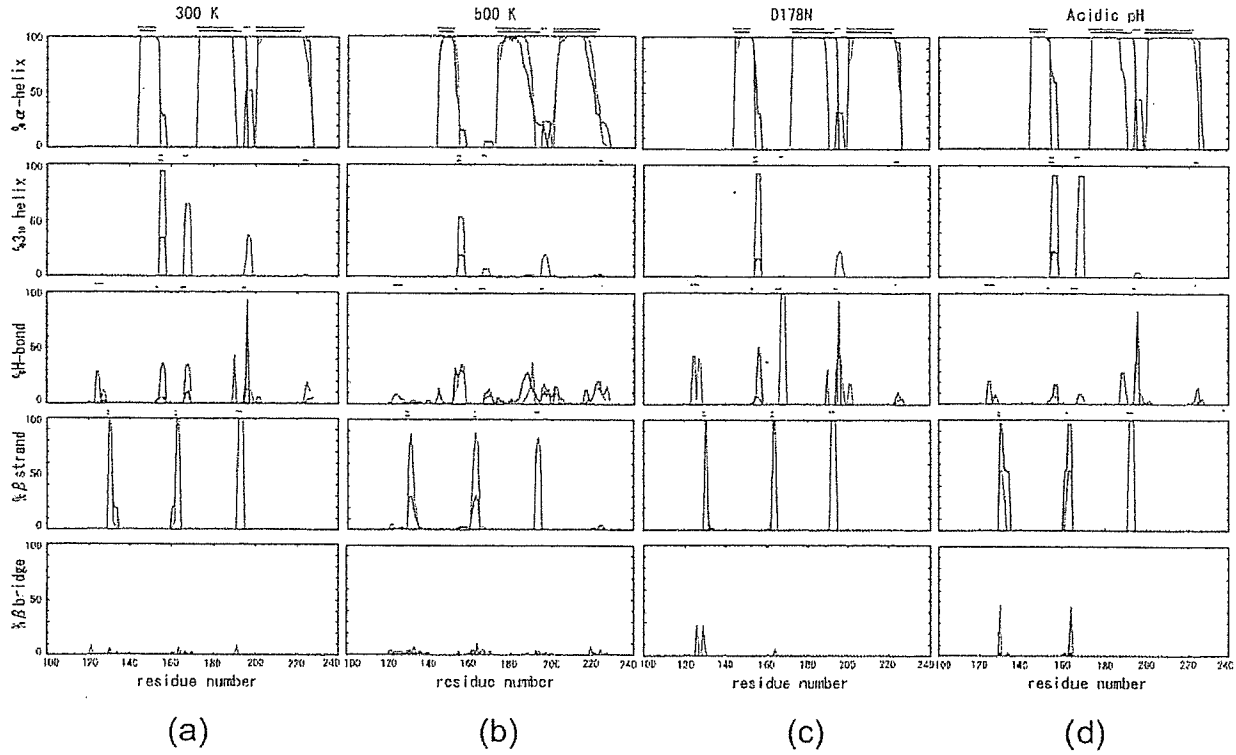

FIGURE 7 Percentage of secondary structure per residue during simulations at (*a*) 300 K, (*b*) 500 K, (*c*) D178N, and (*d*) acidic pH. Red and green indicate the monomer and dimer, respectively. Lines above each figure show the initial structure.

H2 tend to elongate to the C-terminus side whereas H3 exhibited a tendency for elongation to the N-terminus side in the monomer. Fewer S1 and S2 elements were noted in the monomer than the dimer. S1 tended to elongate to the C-terminus side whereas S2 exhibited a tendency for elongation to the N-terminus side in both the monomer and dimer (Fig. 5 *d*).

Many of the secondary structures in both the monomer and dimer were similar at D178N to those observed at 300 K, confirming the Cα RMSD values from the initial structure findings (Fig. 2 *b*). In comparison with 300 K, at D178N residues 167–169 (both ends of the dimeric PrP^c) revealed an H-bond instead of a 3_{10}-helix in the dimer. In the dimer, S1 and S2, but especially monomeric elements, tend to elongate to the C-terminus side and the N-terminus side, respectively.

At acidic pH values, some secondary structures were different from those seen at 300 K (Fig. 7 *d*) and the elongation of H1 in the monomer to the C-terminus side was more pronounced. Dimeric residues 167–169 mainly formed 3_{10}-helices. S1 and S2 in the dimer of chain A decreased probability to form β-sheets and it made β-bridges instead (Figs. 5 *b* and 6 *b*). In both the monomer and dimer, S1 and S2, but especially monomeric elements, tend to elongate to the C-terminus side and the N-terminus side, respectively (Figs. 5 and 6).

Fig. 7 shows that in both the monomer and the dimer but especially in the monomeric elements, S1 and S2 tended to elongate to the C-terminus side and the N-terminus side, respectively, at 300 K and acidic pH.

Positional RMSD from the average structure

Because we were unable to detect major differences in the results obtained at 300 K, D178N, and acidic pH, we present our results obtained with simulations at 300 K and 500 K. Fig. 8 shows Cα RMSD values from the mean structure as a function of residue number and is suitable for describing the flexibility differences among the residues. Because there were few differences between the RMSD profiles of chains A and B in the dimer (data not shown), only chain A is depicted. In order, the Cα RMSD values increased for the dimer at 300 K, the monomer at 300 K, the dimer at 500 K, and the monomer at 500 K. Fluctuations at positions 1 (Arg^{136}), 2 (Phe^{141}), 3 (Tyr^{157}), and 4 (Asp^{168}) were far larger than were fluctuations of other residues. The residues exhibiting the large fluctuations correspond with the loop regions, and at 300 K, only loop regions manifested fluctuations. Interestingly, a region adjacent to position 4 (residues 169–171) is a putative binding site for protein X (Kaneko et al., 1997), and NMR showed it to be flex-

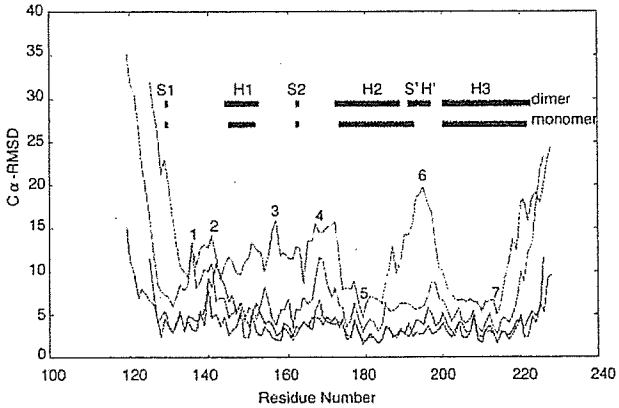

FIGURE 8 Cα RMSD values from the average structure as a function of residue number. Red, blue, green, and pink lines indicate RMSD values of the dimer at 300 K, monomer at 300 K, dimer at 500 K, and monomer at 500 K, respectively.

ible(Viles et al., 2001). Resonances of the loop are not observed in HuPrP due to conformational exchange. At position 6 (Gly^{195}), the Cα RMSD values in the monomer increased to 19.9 Å at 500 K. At the same temperature, the same residue of the dimer increased to only 5.96 Å. This is consistent with Fig. 3 *d*, which shows that S′ and H′ stabilized this region. The smallest fluctuations were observed at positions 5 (Cys^{179}) and 7 (Cys^{214}) in H2 and H3, where residues Cys^{179}–Cys^{214} of the monomer, and Cys^{179}–Cys^{322} and Cys^{214}–Cys^{287} of the dimer are connected by disulfide bridges and contribute to the stabilization of neighboring regions. It appears that H2 and H3 form a relatively stable core of the protein and MD simulations of the prion from Syrian hamster indicated that the remainder of the protein has a degree of conformational plasticity (Parchment and Essex, 2000). Studies that mapped antibodies to various epitopes on PrP (Peretz et al., 1997) also support the hypothesis that a core of the molecule containing H2 and H3 remains intact after the conversion of PrP^{C} to PrP^{Sc}.

Cα contact maps

Analyses of the close contacts throughout the simulations are shown in Fig. 9. The degree of each native contact during the simulations is depicted in red, pink, green, yellow, and blue in decreasing order. In Fig. 9, *a* and *b*, region 1 is the area of contact between S1 and H1 to just after S2, region 2 facilitates contact between S2 and H2, region 3 between H2 and H3, region 4 from the loop just after H1 to the loop connecting S2 with H2, and in region 5, contact occurs between the area just before S1 to H1 and H3. Monomers and dimers share many similarities in these regions. Regions 6 and 7, however, are unique to the dimer and comprise the dimer interface. Region 6 is the contact between H1 of chain A and H1 of chain B, and region 7 provides for contact between H′ and S′ of chain A and their counterparts in chain B. Fig. 9 *d* shows that during simulation at 500 K, most of the native interactions in the dimer lasted longer than those in the monomer (Fig. 9 *b*).

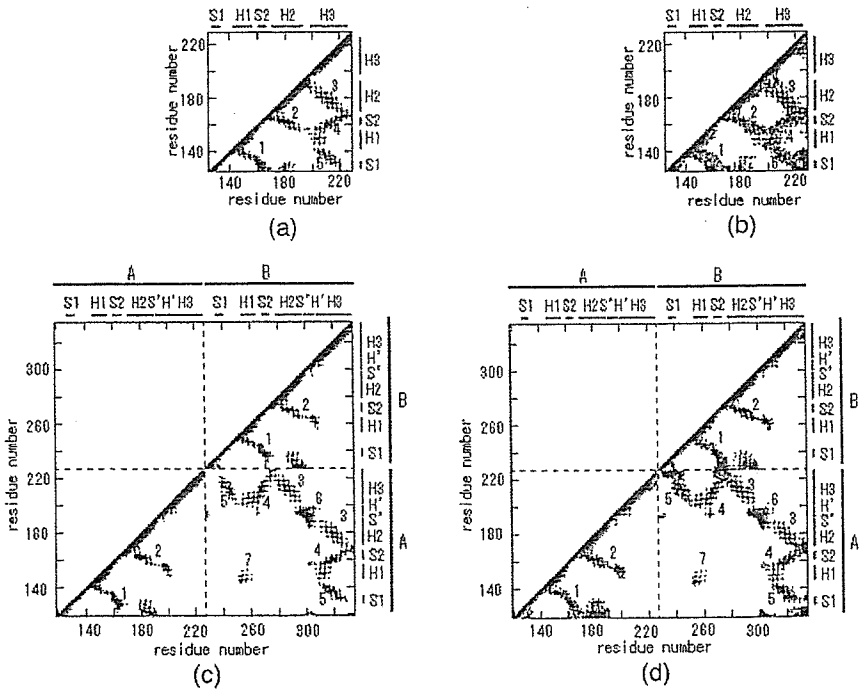

FIGURE 9 Cα contact maps. (*a*) Monomer at 300 K; (*b*) monomer at 500 K; (*c*) dimer at 300 K; and (*d*) dimer at 500 K. The distance of Cα was 11 A. The existence ratio of contact 0–20% is shown in blue, 20–40% in yellow, 40–60% in green, 60–80% in pink, and 80–100% in red.

SUMMARY

PrP exists in not only a monomeric but also a dimeric form (Meyer et al., 2000; Knaus et al., 2001). Recent models suggest that dimerization plays an important role in the conformational change of PrP^C to PrP^{Sc} (Tompa et al., 2002). Although earlier MD simulations have yielded information on the monomeric form of PrP^C, data on its dimeric form remain scarce. To elucidate the conformational change of PrP^C to PrP^{Sc}, the dynamics of the dimeric form of PrP^C must be known. Therefore, we performed totally monomeric 40-ns simulations and dimeric 40-ns simulation in various conditions. Our conclusion that the monomer started denaturing earlier than the dimer is based on results we obtained in our study of Cα RMSD values from the initial structures (see Fig. 2), of secondary structure evolution during simulation (see Fig. 3), and of structures representative of conformational changes (see Fig. 5). Our results also showed that α-helices in both the monomer and dimer denatured in a similar manner (see Fig. 3). As the rate of protein denaturation is molecular weight-dependent, the greater retention of dimeric than monomeric tertiary and secondary structures is expected. However, we observed that in the dimer, the helices were denatured more readily whereas the tertiary structure was retained more than in the monomer. This suggests that the dimer interface, H' helices (residues 194–197 and 302–305), and an S' β-sheet (residues 191–193 and 299–301) play an important role in the inhibition of tertiary structure of denaturalization. Although the discussion above was based on the simulation at 500 K, which was performed only one time for each prion model, the results potentially have biological importance. In our simulations, S1 and S2 in the dimer and especially the monomer tended to elongate to the C- and N-terminal sides, respectively, under most of the experimental conditions (see Figs. 4–7). This suggests that the monomeric form of PrP^C is more likely to gain β-sheets. Our results suggest that if dimerization plays an important role in the transition from PrP^C to PrP^{Sc}, some factors are required to enhance it. Kaneko et al. (1997) posited the existence of a molecular chaperone, protein X, and Tompa et al. (2002) proposed a disulfide-reshuffling model that is based on contacts between PrP^C and PrP^{Sc} dimers and disulfide rearrangement(s). Our simulations were performed mainly on the well-ordered part of $HuPrP^C$ (residues 125–228 in the monomer and 119–226 and 227–334 in the dimer, termed the C-terminal region). In addition, N-terminal residues 90–124, truncated in the present model, are required for α-helix-to-β-sheet transition and for prion disease infectivity (Prusiner, 1982; Pan et al., 1993; Muramoto et al., 1996). Current simulation models will continue to yield insights into the structure, function, and dynamics of PrP, and work is continuing in our laboratory to elucidate the dynamics, structural change(s), and other factors that involve the monomeric and dimeric forms of PrP.

CONCLUSION

Ours is the first reported exploration of the dynamics of dimeric PrP^C, residues 119–226, using MD simulation to assess whether the dimer is essential for the conformational transition of PrP^C to PrP^{Sc}. Our results showed that denaturation of helices and elongation of the β-sheet were common to both the monomer and dimer. However, additional secondary structure elements formed in the dimer might result in the greater retention of dimeric than monomeric tertiary structure. Our results suggest that if dimerization plays an important role in the transition from PrP^C to PrP^{Sc}, some factors are required to enhance it. At present, we cannot rule out the possibility that dimerization of HuPrP is a necessary step in the transition from PrP^C to PrP^{Sc}. Efforts are under way in our laboratory to perform simulations of PrP 27–30, residues 90–231, to gain a better understanding of the underlying process(es) of conformational change from PrP^C to PrP^{Sc}.

The authors thank Dr. M. Gromiha, Dr. S. Nakamura, Dr. K. Shimizu, Dr. M. Suwa, and Dr. T. Hirokawa for helpful discussions.

REFERENCES

Berendsen, H. J. C., J. P. M. Postma, W. F. Vangunsteren, A. Dinola, and J. R. Haak. 1984. Molecular-dynamics with coupling to an external bath. *J. Chem. Phys.* 81:3684–3690.

Berman, H. M., T. N. Bhat, P. E. Bourne, Z. Feng, G. Gilli, H. Weissig, and J. Westbrook. 2000. The Protein Data Bank and the challenge of structural genomics. *Nat. Struct. Biol.* 7:957–959.

Case, D. A., D. A. Pearlman, J. W. Caldwell, T. E. Cheatham III, J. Wang, W. S. Ross, C. L. Simmerling, T. A. Darden, K. M. Merz, R. V. Stanton, A. L. Cheng, J. J. Vincent, M. Crowley, V. Tsui, H. Gohlke, R. J. Radmer, Y. Duan, J. Pitera, I. Massova, G. L. Seibel, U. C. Singh, P. K. Weiner, and P. A. Kollman. 2002. Assisted Model Building with Energy Refinement 7 (AMBER 7). University of California, San Francisco, CA.

Cohen, F. E., K.-M. Pan, Z. Huang, M. Baldwin, R. J. Fletterick, and S. B. Prusiner. 1994. Structural clues to prion replication. *Science.* 264:530–531.

Cornell, W. D., P. Cieplak, C. I. Bayly, I. R. Gould, K. M. Merz, Jr., D. M. Ferguson, D. C. Spellmeyer, T. Fox, J. W. Caldwell, and P. A. Kollman. 1995. A second generation force field for the simulation of proteins, nucleic acids, and organic molecules. *J. Am. Chem. Soc.* 117:5179–5197.

Darden, T., L. Perera, L. Li, and L. Pedersen. 1999. New tricks for modelers from the crystallography toolkit: the particle mesh Ewald algorithm and its use in nucleic acid simulations. *Structure Fold. Des.* 7:R55–R60.

Darden, T., D. York, and L. Pedersen. 1993. Particle mesh Ewald: an N·log (N) method for Ewald sums in large systems. *J. Chem. Phys.* 98: 10089–10092.

Day, R., B. Bennion, S. Ham, and V. Daggett. 2002. Increasing temperature accelerates protein unfolding without changing the pathway of unfolding. *J. Mol. Biol.* 322:189–203.

Donne, D. G., J. H. Viles, D. Groth, I. Mehlhorn, T. L. James, F. E. Cohen, S. B. Prusiner, P. E. Wright, and H. J. Dyson. 1997. Structure of the recombinant full-length hamster prion protein PrP(29–231): the N terminus is highly flexible. *Proc. Natl. Acad. Sci. USA.* 94:13452–13457.

El-Bastawissy, E., M. H. Knaggs, and I. H. Gilbert. 2001. Molecular dynamics simulations of wild-type and point mutation human prion